8-8-2023

# Exploration of Miniature Flexible Devices Empowered by Van Der Waals Material

Ningxin Li

Exploration of Miniature Flexible Devices Empowered by Van Der Waals Material

by

Ningxin Li

Under the Direction of Sidong Lei, PhD

A Dissertation Submitted in Partial Fulfillment of the Requirements for the Degree of

Doctor of Philosophy

in the College of Arts and Sciences

Georgia State University

2023

ABSTRACT

This research mainly focuses on the fabrication of miniature flexible devices empowered by van der Waals materials. Through the extensive experiments contained in this thesis, by exploring the characteristics of van der Waals materials, optimizing the manufacturing process of lithography technology, and characterizing the photoelectric performance of micro devices, this thesis has promoted the development of micro flexible device manufacturing and expanded its applications in the fields of biological detection, medical treatment, and environmental monitoring. We introduced a miniature van der Waals semiconductor empowered vertical color sensor, which saves three times the volume space compared to the traditional planer color sensor and includes multiple optical aberration correction functions as well. Such a small red, green, and blue (RGB) color sensor can be applied in bionic eyes, breaking through the limitations of existing black and white recognition. On this basis, we further explored the stretchability of two-dimensional materials represented by $MoS_2$. We proposed a chemical treatment method combined with gold nanoparticles and (3-mercaptopropyl)trimethoxysilane (MPTMS) to realize the relocation of flexible micro devices. This method improves the adhesion between the material layer and the flexible substrate (PDMS), which significantly increases the flexible device stretchability, and prolongs its service life. Through the above work, this thesis explores the van der Waals materials' properties, and optimizes the manufacturing process of micro devices, further exerts the advantages of material flexibility, therefore provides more possibilities for the development of smart wearable devices, biomedical detection, and other fields.

INDEX WORDS: Van der Waals, Miniaturization, Color sensor, Flexibility, $MoS_2$, MPTMS

Exploration of Miniature Flexible Devices Empowered by Van Der Waals Material

by

Ningxin Li

Committee Chair:     Sidong Lei

Committee:     Vadym M Apalkov

Mukesh Dhamala

Unil A G Perera

Electronic Version Approved:

Office of Graduate Services

College of Arts and Sciences

Georgia State University

August 2023

**DEDICATION**

For Guilian Liu, Changyong Li

# ACKNOWLEDGEMENTS

vi

Thanks to Dr. Gangli Wang for advice on chemical treatment method of strain engineering part and his support for my postdoc application.

Thanks to my collaborators Ruoyu Yang, and Hedi Ma, who are from chemistry department for all the discussions.

Special thanks to my dear friends Qiantong Guo, Peiyuan Wang, Yingzi Liu, Xiaobei Xu, Zhongyi Sheng, Chiqu Li, Ruxin Li, Meiqi Lin, Lingchao Mao, Wan Li, Tengfei Bai, Yuxuan Yang, and Wenbo Liu, for believing in me always and supporting me in all hard times.

Special thanks to my lovely bunny Jizi Peng, who always supported me unswervingly, comforted and hugged me at countless times when I felt pressured and collapsed, that really means a lot.

Thanks to my wonderful parents, I would not be able to achieve anything without their support.

Thanks to my cousins, aunts, uncles, they always believe in me and support me.

Thanks to my lab mates, Aisha Okimi, Tara Jabegu, and Diren Maraba, for their help and support.

Very special thanks to the National Science Foundation (NSF) for the funding support. This is the prerequisite for the success of all my doctoral projects. Without it, there would be no such amazing results.

Very special thanks to the faculty start-up funding provided by Georgia State University, which ensured the smooth development of the research.

**TABLE OF CONTENTS**

# LIST OF FIGURES

# LIST OF ABBREVIATIONS

Van der Waals Semiconductor (vdW-S)

Two Dimensional (2D)

Chemical Vapor Deposition (CVD)

$CuIn_7Se_{11}$ (CIS)

Color Correction Matrix (CCM)

Chanel Selection (CS)

Pixel Selection (PS)

Focus Ion Beam (FIB)

Polydimethylsiloxane (PDMS)

(3-mercaptopropul) Trimethoxy Silane (MPTMS)

Atomic Force microscopy (AFM)

Complementary Metal-Oxide-Semiconductor (CMOS)

Poly(methylmethacrylate) (PMMA)

Polydimethylglutarimide (PMGI)

# 1  INTRODUCTION

## 1.1  Van Del Waals Semiconductor Background

Van der Waals semiconductor (vdW-S) materials are very common and important sources of microelectronic raw materials. Van der Waals interaction (vdW) is named after the Dutch scientist Johannes Diderik 'van der Waals'[1]. With the continuous development of two-dimensional(2D) atomic crystals without dangling bonds such as graphene, different 2D atomic layers can be stacked together in a specific order by means of weak van der Waals forces to construct various heterostructures with atomically flat interfaces[2]. The structure is called a van der Waals heterostructure.

Van der Waals semiconductors are physically assembled together by relatively weak van der Waals interactions. Compared with traditional semiconductor heterojunctions, van der Waals semiconductors do not depend on chemical bonds and are not limited by the lattice matching of materials. In principle, if there are no special requirements for lattice similarity and processing compatibility[3], this van der Waals semiconductor integration strategy is applicable to any material, especially for the flexibility of materials with different crystal structures, different electronic properties, different sizes and dimensions integrated. For modern electronics and optoelectronics, semiconductor heterojunctions and superlattices provide a broad research platform for the development of new electronic and optoelectronic devices. Integrating disparate materials together to construct a new interface is a crucial step in designing functional devices, and it has been a long-standing pursuit of material scientists.

## 1.2  The Flexibility of Van Der Waals Semiconductors

In 2004, when several physicists, including Andrew Geim and Konstantin Novoselov, obtained graphene from graphite[4], the entire material science community was deeply shocked.

This kind of material, which has been predicted by theorists as impossible to exist, not only can exist stably, but also has extremely high mechanical strength and electrical conductivity. For the first time, people have seen that a material a single atom thick can be strong enough to be suspended in the air without breaking. Such properties of graphene are inseparable from its microscopic structure can be seen in Fig. 1[5]. Following the path of graphene, the door to 2D materials is suddenly opened. From graphene as a conductor, to semiconductor $MoS_2$, insulator h-BN, superconductor $NbSe_2$, ferromagnet $CrI_3$, etc., they all have common characteristics, that is, the atoms in the layer are connected by covalent bonds, and the layers are connected by van der Waals force. The discovery of 2D materials provides a new idea for creating new heterostructures. 2D material has a stronger mechanical strain bearing capacity because of its thin thickness and lack of dangling bonds. It is no doubt that 2D materials will play a pivotal role in the flexible wearable devices because of these excellent mechanical properties[6]. Even better, due to the flexibility of 2D materials, various devices processed by such heterojunctions have very good ductility and bendability and have broad application prospects in the field of flexible electronics[7](Fig. 2).

## 1.3    The Micro Fabrication Techniques

Micro fabrication technology refers to submillimeter, micron and nanoscale components and the optimized design, processing, assembly, system integration and application technology of components or systems composed of these components. It involves a wide range of fields and multidisciplinary integration. Micro-nano devices and systems are a series of special technologies developed in the manufacture of integrated circuits. The term 'lithography' refers to a process invented by Aloys Senefelder in 1796[8]. He found that if he used Bavarian limestone and applied the appropriate ink, after a series of chemical treatments, the engraved image can be transferred to

paper[9]. This is the prototype of the earliest photolithography technology. Micro-nano processing technology based on photolithography mainly includes the following processes: mask (mask) preparation, pattern formation and transfer (coating, exposure, development), thin film deposition, etching, epitaxial growth, oxidation, and doping, etc. Coat a layer of photosensitive medium film (resist) on the surface of the substrate. The exposure system projects the pattern of the mask on the (resist) film. The light (photon) exposure process makes the resist undergoes photochemical action to form a latent image of a fine pattern, and then the remaining resist layer is transformed into a window with a fine pattern through the development process, and the subsequent coating and etching based on the resist pattern can further produce the desired microscopic pattern, nanostructures or devices. The development of devices and systems such as micro-sensors and micro-actuators has the distinctive characteristics of miniaturization, batch production, and low cost. It has a huge impact on modern life and production. The role of promotion and gave birth to a number of new industries.

## 2    CHAPTER 2 VAN DEL WAALS SEMICONDUCTORS

Manipulating different atoms to stack one by one to obtain the desired material has always been one of the ultimate dreams of chemists. The discovery of single-atom-thick graphene in 2004 brought hope to such a dream. For more than ten years, along this road, people have successively found semiconductors with atomic thickness. Since then, people can simply stack these materials like building walls to obtain a large number of van der Waals heterojunctions with very different functions. In future applications such as integrated circuits, photodetectors, and sensors, these van der Waals heterojunctions with rich functions will surely play an important role, helping people move towards the era of the internet of everything. In this chapter, we will introduce vdW-S as a miniature electronic device in detail from its historical development, synthesis methods, and its excellent optoelectronic and mechanical properties.

### 2.1    Van Del Waals Semiconductor Background

As we mentioned in the introduction, after the single-layer graphene has been successfully exfoliated, 2D materials have become a hot new material in the eyes of physicists. They stack together through the weak interactions between atoms and thus forming a vdW-S heterojunction. The superior optoelectronic properties exhibited by them have enabled the continuous expansion of the functional scope and application fields of these heterostructure materials. The discovery of 2D materials provides a new idea for creating new heterostructures. In the past, heterojunctions could be obtained by doping homogeneous materials, such as the PN junction of semiconductor silicon, or by epitaxial growth on a lattice-matched substrate material[10]. This method has very serious restrictions on the material, and serious dislocations and defects will be formed at the interface if you are not careful, which will affect the quality of

the heterojunction. However, this problem does not exist for 2D materials. Since there is no covalent bond between the layers, it is not limited by lattice matching and material types, and a perfect heterojunction can be obtained by sequentially stacking different materials. Moreover, the perfect heterostructure brings perfect electrical properties as well. For example, the stacked metal-semiconductor heterojunction has very few interface defects, and the Fermi level pinning is released, making the interface barrier height tend to the Schottky-Mott limit[11]. Even better, due to the flexibility of 2D materials, various devices processed by such heterojunctions have very good ductility and bendability, and have broad application prospects in the field of flexible electronics.

After understanding the nature of van der Waals heterojunction, we can think of: not only 2D materials, but also zero-dimensional nanoparticles, one-dimensional nanowires and nanorods, and even three-dimensional materials, any two materials that interact with van der Waals force materials, we can all make them stack together in a certain way, forming van der Waals heterojunctions. This series of methods can be collectively referred to as van der Waals integration[12]. In future microelectronic devices, we can use van der Waals integration to greatly reduce manufacturing costs while improving performance. Semiconductor channels, metal electrodes, interconnects, photodetectors, memory, and even isolation and packaging layers can all be obtained by stacking layers. Perhaps one day in the future, integrated circuits will move out of tens of billions of dollars of investment in semiconductor factories and become a product that can be manufactured in a printing factory.
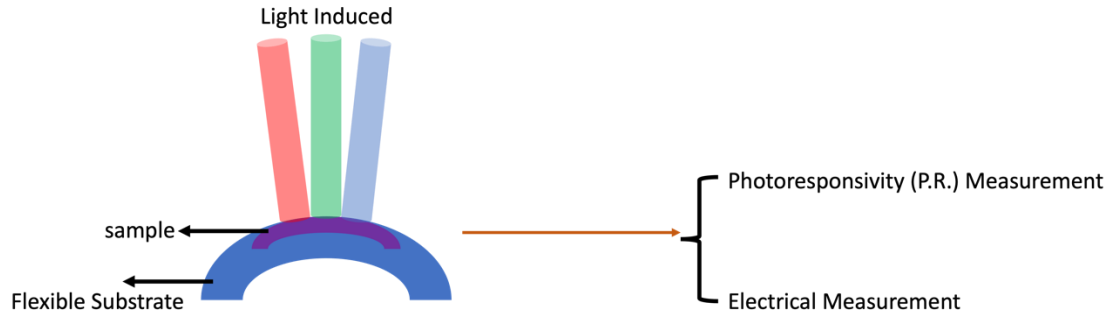
*Figure 2.1 Optoelectronic characterizations of the flexible and stretchable device.*
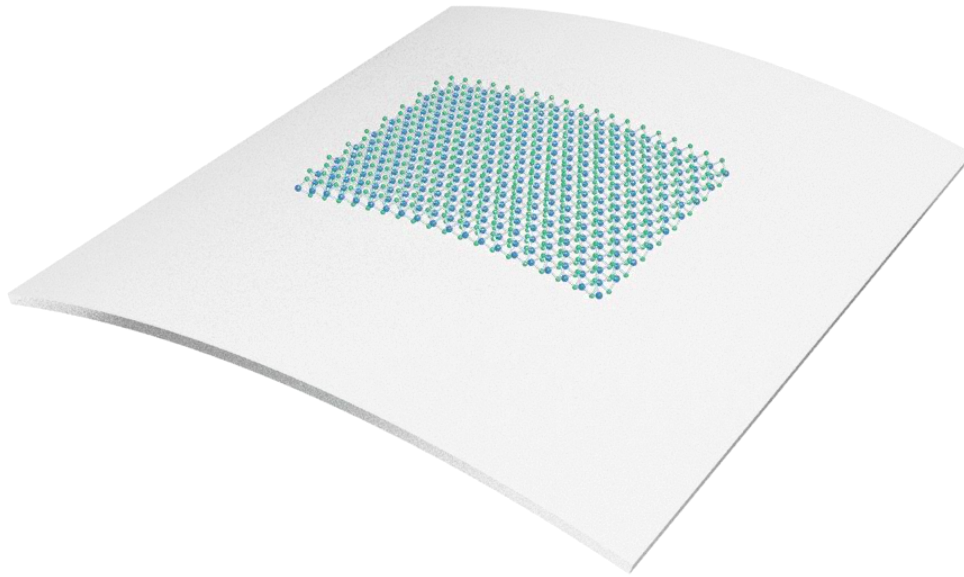


*Figure 2.2 2D materials on flexible substrate.*

## 2.2  Growth of Van Del Waals Semiconductor

To successfully stack heterostructures, we first need to synthesis vdW-S. The growth and synthesis of vdW-S are important parts of microelectronics manufacturing. The quality of the synthesized samples will directly affect its photoelectric performance. At present, the common growth of atomic thickness vdW-S is mainly chemical vapor deposition(CVD), which represented by graphene[13]. Besides that, here, we will list several synthetic methods of

common vdW-S that are involved in the research of the miniature color sensor described in chapter 3 in this thesis, more information can refer to 3.4.2:

GaS: A tube furnace consisting of two temperature-controlled zones was used for GaS crystal growth. We kept the temperature in two zones at 950 and 450 °C for 24 hours. Among them, gallium is located in the 950 °C region. Then, the tube was cooled naturally until it reached room temperature[14].

InSe: The high-quality bulk InSe crystals were synthesized using a nonstoichiometric melt consisting of indium (>99.99%, Alfa Aesar Co.) and selenium (>99.99%, Sigma-Aldrich Co.)[15]. The indium and selenium were mixed in a molar ratio of 52:48 and placed in a quartz tube under vacuum ($10^{-3}$ Torr). The precursor was heated to 685°C and held at that temperature for 3 hours to ensure complete reaction between the indium and selenium. Subsequently, following the phase diagram of the InSe system, the temperature was raised to 700°C and maintained for another 3 hours to obtain a uniform InSe melt. The melt was then gradually cooled from 700°C to 500°C with 20hrs, and further cooled naturally over 6 hours to room temperature, resulting in high-quality InSe crystals.

The growth of $CuIn_7Se_{11}$ can refer to the references[16].

## 2.3    Van Del Waals Semiconductor's Characters

### 2.3.1    Mechanical Characteristic

As mentioned earlier, multilayer van der Waals materials such as graphene, hexagonal boron nitride (h-BN), transition metal sulfides ($MoS_2$, etc.) and their heterojunctions are a new class of thin materials consisting of several thin layers of the same or different covalently bonded atoms are linked by weak van der Waals interactions. Multilayer van der Waals materials usually

have extremely high in-plane stiffness, low interlayer shear modulus, and extremely low single-layer bending stiffness due to the highly anisotropic atomic layer structure, which makes them more flexible with superior out-of-plane deformation properties, easy to form curls, bubbles, folds[17].This remarkable mechanical behavior makes multilayer van der Waals materials widely used in bending-related fields, such as flexible electronics and sensors, wearable devices, flexomagnetic effects, etc.

### 2.3.2 *Optoelectrical Characteristic*

2D layered materials have attracted increasing attention from researchers due to their novel electronic/optoelectronic properties and high compatibility with silicon-based technologies. When the flake thickness of 2D materials is reduced to the atomic level, their optoelectronic performance will show great advantages. Adjustable bandgap width[14] and rich material types can realize full-range photodetection (from ultraviolet to infrared). In addition, different 2D materials can be stacked freely by means of weak van der Waals forces to form artificial heterostructures with atomically flat interfaces, which are often called van der Waals heterojunctions[18]. By choosing different 2D materials and specific stacking methods, their unique properties can be organically combined. From this research perspective, van der Waals heterojunctions provide a new platform to study the properties of novel electronic and optoelectronic devices.

To sum up, the use of vdW-S to manufacture microelectronic devices is closely related to its own material properties. The details of the characterization of the optoelectrical characteristic of vdW-S will be described in detail in chapter 3 and the characterization and improvement of the flexibility/ductility of vdW-S will be described in detail in chapter 4 of this thesis. However, whether it is synthetic growth or the research on the material itself, it is of great significance to

determine and improve the performance of microelectronic devices, which is also the purpose of

starting the thesis by using this chapter.

# 3    CHAPTER 3 MICRO FABRICATION TECHNIQUES

Micro fabrication technology is an emerging comprehensive processing technology. It integrates advanced technological achievements such as modern machinery, optics, electronics, computers, measurement, and materials, and improves the processing accuracy from the micron level in the early 1960s to the current 10nm level, which has increased by 1 to 2 orders of magnitude in decades, greatly improving the performance and reliability of the product. Micro fabrication processing can be roughly divided into two categories: "top-down" and "bottom-up". "Top-down" starts from the macro-object and processes materials or raw materials based on the lithography process. The minimum result size and precision are usually determined by the resolution of the lithography or etching process. "Bottom-up" technology starts from the microscopic world and builds various units together by controlling the interaction force of atoms, molecules and other nano-objects to form micro-nano structures and devices. In this chapter, we will introduce the microelectronics fabrication technology in detail, to enable readers to have a broader and deeper understanding of the development and application of the semiconductor processing industry.

## 3.1    Background and Development

### 3.1.1    Semiconductor Moore's Law

Moore's Law is proposed by Gordon Moore, one of the founders of Intel. Its core content is that the number of transistors that can be accommodated on an integrated circuit will double approximately every 18 to 24 months[19]. In other words, the performance of processors doubles approximately every two years, while the price drops by half. "Moore's Law" summarizes the speed at which information technology advances. In the more than 50 years since the application

of Moore's Law, the computer has changed from a mysterious and inaccessible behemoth to an indispensable tool for most people, information technology has entered countless ordinary families from laboratories, the Internet has connected the world, and multimedia audio-visual equipment has enriched everyone's life. "Moore's Law" has far-reaching implications for the entire world. When reviewing the progress of the semiconductor chip industry over the past 40 years and looking forward to its future, information technology experts believe that "Moore's Law" may still apply in the future. But this law will eventually come to an end as transistor circuits approach their performance limits. For more than 40 years, the integration trend of semiconductor chips, as predicted by Moore, has promoted the development of the entire information technology industry, and brought changes to the lives of thousands of households.

### 3.1.2   *Historical Developments of Micro Fabrication*

After transistor was invented in 1947, the micro fabrication revolution was sparked[9]. Photolithography is the soul technology of micro fabrication manufacturing. It is the emergence of photolithography that brought the manufacture of silicon devices into the era of planar processing technology, and the rapid development of large-scale integrated circuits and microelectronics today.

The invention of photolithography in a general sense should be traced back to the photosensitive material experiment and etching experiment of the French scientist Joseph Nicephore Niepce in 1822[20]. The specific invention time of lithography technology has always been debated, there are very few references which recorded it. However, there are mainly two theories are well known. The first one is that in 1960, H.H.Loor and E.Castellani invented the photolithography process. The second argument is that in 1970, E.Spiller and E.Castellani invented the photolithography process[21, 22]. There is a 10-year difference between the

invention of lithography in the two versions. The author believes that 1960 should be the year when the lithography process was invented. If the lithography process was invented in 1970, then in the ten years from 1958 to 1970, the semiconductor products (bipolar, FET, MOSFET, etc.) of pioneer companies such as Bell Labs, Fairchild, TI, RCA and Intel transistors) and chips are difficult to manufacture.

The author also believes that Fairchild should be the place where photolithography was invented. In 1958, several founders of Fairchild purchased three 16mm lenses from a camera store, made a step-and-repeat camera device, used it to make masks, and improved the mask and photoresist. In 1959, Robert Noyce (Robert Noyce) put forward a technical idea in his diary, "Since photolithography can be used to manufacture a single transistor, why can't photolithography be used to mass-produce transistors?", " Putting the components on a single silicon chip will enable the interconnection of the components in the process flow, so that the size and weight will be reduced, and the price will also be reduced." To this end, Fairchild began to try to apply photolithography to mass production of transistors. Noyce put forward the idea of "plane technology", and Jean Hoerni is the master who transformed this idea into a practical "plane processing" technology[19, 23].

On the other hand, from the perspective of the development era of lithography machines, in the 1960s, it was a contact lithography machine and a proximity lithography machine. In the 1970s it was a projection lithography machine. In the 1980s, it was a stepping lithography machine, type scanning lithography machine, immersion lithography machine and the current EUV lithography machine[24-26]. Hence, the lithography process for micro fabrication may have been invented earlier than 1970 with a greater probability.

Without lithography technology, there would be no chip technology and industry today, and there would be no information and intelligent society today.

## 3.2   Standard Fabrication Workflow

Micro fabrication technology based on photolithography mainly includes the following processes: mask (mask) preparation, pattern formation and transfer (coating, exposure, development), thin film deposition, etching, epitaxial growth, oxidation, and doping, etc. Since the work of this thesis is related to the fabrication of independent micro devices, we will focus more to the process from mask preparation to thin film deposition.

Firstly, researchers coat a layer of photosensitive medium film (resist) on the surface of the substrate, then the exposure system projects the pattern of the mask on the (resist) film. The light (photon) exposure process makes the resist undergoes photochemical action to form a latent image of a fine pattern, and then the remaining resist layer is transformed into a window with a fine pattern through the development process, and the subsequent coating and etching based on the resist pattern can further produce the desired microscopic pattern. nanostructures or devices.

### 3.2.1   Mask Preparation

The mask is a template with a transparent window prepared from the enlarged original image (Fig. 3). For example, a flat glass plate can be coated with a metal chromium film and prepared by a method similar to photoengraving[27, 28]. A mask with a micro-nano pattern structure is usually directly prepared by an electron beam lithography machine. The production process is a typical photolithography process, including metal layer deposition, resist coating, electron beam lithography, development, chromium layer corrosion and removal. Due to the large

number of template pixels, the speed of making a mask with a scanning lithography machine is quite slow and the cost is very expensive.
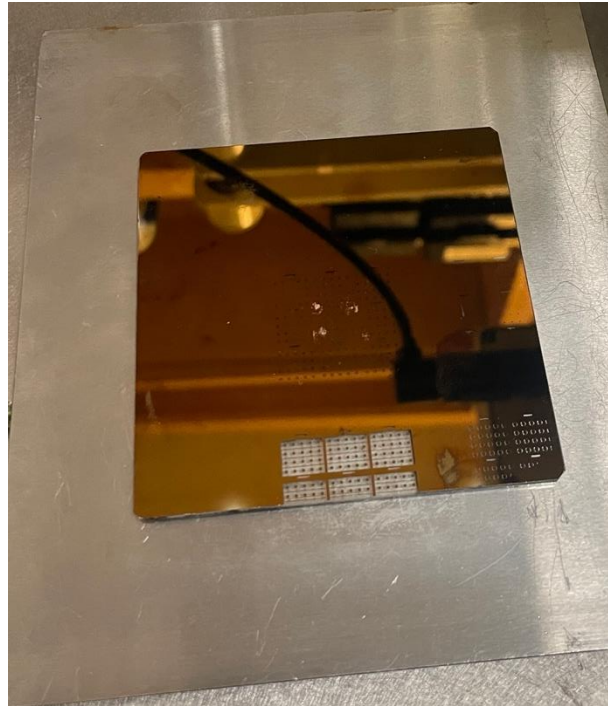


*Figure 3.1 Lithography mask.*
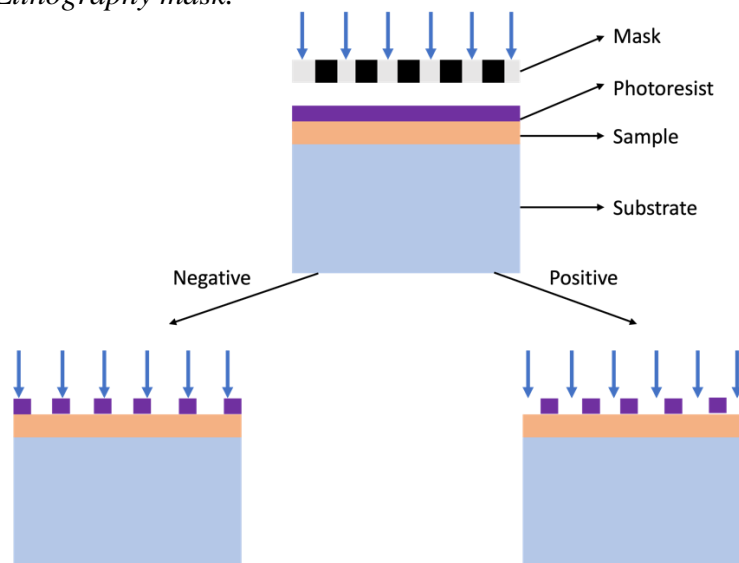


*Figure 3.2 Lithography principle of photoresist.*

### *3.2.2   Exposure*

Exposure lithography is the core process of pattern formation, which can be divided into positive resist process and negative resist process[29] (Fig. 4). When the same mask is used for production, these two can obtain complementary pattern structures. In addition, according to different working distances, it can be divided into proximity exposure, close exposure (contact exposure) and projection optical exposure. And according to the working light source of the exposure system, it can be divided into ultraviolet exposure, electron beam and ion beam exposure. The exposure machine which used for fabricating the pattern of the micro device in chapter 4 is an ultraviolet contact exposure (Fig. 5). Moreover, the high-precision microstructures can be produced by electron beam direct writing or laser direct writing. This type of lithography technology, like "writing", exposes by controlling the focused electron beam (beam) to move the writing pattern, which has high exposure accuracy. However, the production efficiency of these two methods is extremely low, especially in large-area production. At present, direct writing lithography technology is only suitable for small-area micro-nano structure production. The exposure machine which used for fabricating the pattern of the micro device in chapter 3 is a laser direct writing system (Fig. 6).
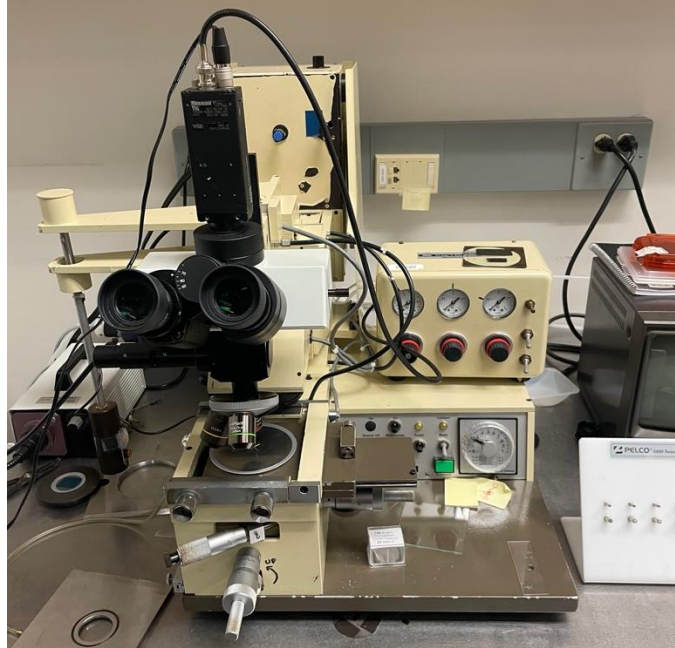
*Figure 3.3 Mask aligner.*
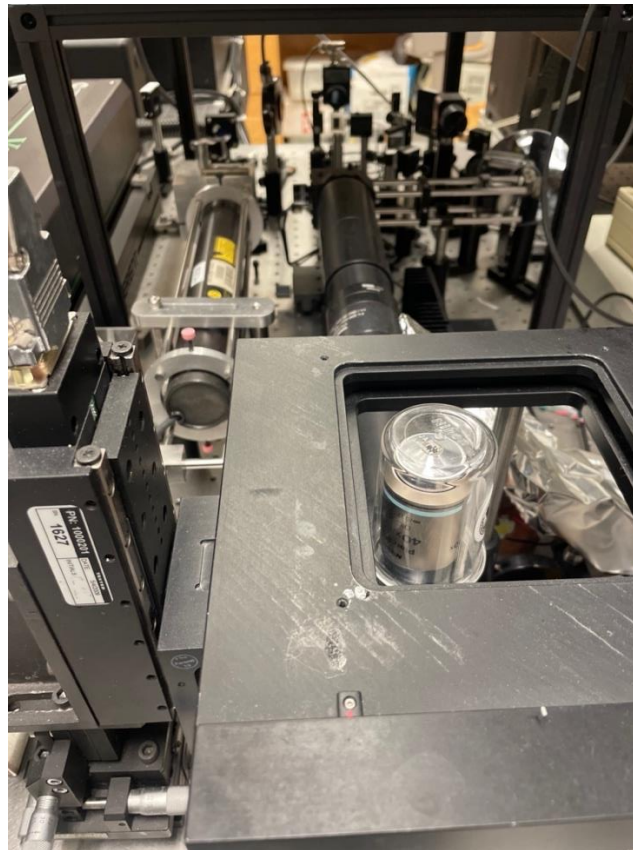


*Figure 3.4 Laser direct writing system.*

### *3.2.3   Deposition*

In the integration of microelectronics and optoelectronics, there are two main types of

thin film formation methods, deposition, and epitaxial growth. Deposition techniques are divided

into physical deposition, chemical deposition, and mixed method deposition. Evaporation

deposition (thermal evaporation, electron beam evaporation) and sputter deposition are typical

physical methods; chemical vapor deposition is a typical chemical method; plasma enhanced

chemical vapor deposition is a hybrid method combining physical and chemical methods.

Epitaxial growth is essentially a thin film processing method in material science, which means:

on a single crystal substrate, a crystalline thin layer with the same or similar crystal structure as

the base is grown directional. Other thin film forming methods, such as electrochemical

deposition, pulsed laser deposition, sol-gel method, self-assembly method, etc., are also widely

used in micro-nano manufacturing processes. All micro devices in this thesis are obtained by

thermal evaporation method (Fig. 7).



*Figure 3.5 Thermal evaporator.*

### 3.3    Micro Fabrication Applications

With the further popularization of modern electronic technology, microelectronics manufacturing has been applied in many aspects of human life. With the advent of the explosion of information and knowledge, products based on micro fabrication technology affect every aspect of our lives, such as our most commonly used communication tools—mobile phones, IC cards for commuting to and from work, laundry, etc[30, 31]. Fully automatic washing machine for eating, rice cooker for cooking, electric kettle for boiling water, and TV programs for enjoying after dinner. These electronic products, which are closely related to our lives, are processed by micro fabrication technology to complete their functional performance, which brings convenience and high-quality enjoyment to our life and have a positive impact on improving our quality of life. Besides that, with the rapid development of social economy, it has brought good opportunities to the industrial manufacturing industry. Facing the advent of the global industrial revolution, the traditional and backward industrial production and manufacturing models are difficult to meet the needs of social production. In order to quickly adapt to the development trend of the industrial industry in the new era, many industrial manufacturing enterprises are actively introducing equipment supported by micro fabrication technology to improve the production efficiency and product accuracy of the enterprise, so as to improve the market competitive advantage, and then realize the long-term development of the enterprise. For example, in the automobile manufacturing industry, monitoring systems and anti-theft systems supported by microelectronics technology[32, 33]. The electronic engine monitoring system has been developed through the integration of microelectronics, which effectively solves the problem that the engine is not easy to control, but the microelectronic

technology is integrated into the monitoring system of the car. Once the car is stolen, the electronic anti-theft system will immediately send out an alarm.

Among the topics studied in this thesis, we pay more attention to the application of microelectronics manufacturing technology in biomedicine[34], such as smart wearable devices, flexible electronic devices, medical imaging therapy, and environmental monitoring. Flexible biosensor is a very hot topic recently, and micro fabrication is an important basis for realizing flexible biosensor. Being able to improve its manufacturing process and optimize parameters can reduce production costs. This is also one of the topics covered in this paper, which will be described more in Chapter 4.

# 4    CHAPTER 4 VAN DEL WAALS EMPOWERED MICRO DEVICE

Micro electromechanical system refers to a micro device or micro device array that can be mass-produced and integrates micro-mechanisms, micro-sensors, micro-actuators, signal processing and control circuits, and interfaces, communications, and power supplies. It involves many disciplines such as electronics, machinery, materials, manufacturing, information and automatic control, physics, chemistry and biology, and integrates many cutting-edge achievements in today's scientific and technological development. Micro device can perform precise operations in tiny spaces that traditional instruments cannot reach, and realize real-time monitoring, so they have a wide range of applications in biomedicine, such as precise drug injection, clinical monitoring, microsurgery, and micro-implantation systems.

Among all the above research areas, the field about bionic eyes is a subject of great humanistic significance. Biomimetic electronic vision systems[35], artificial visual memories inspired by the brain[36], and various other strategies for simulating and perceiving visual information have gained significant attention in conjunction with advancements in artificial intelligence[37, 38], microrobotics[39, 40], and prosthetic devices[41]. However, the present research primarily focuses on monochromatic optoelectronic designs, despite the fact that color plays a crucial role in simulating vision processes, particularly in tasks such as lesion and tissue inspection[42], blood oxygen level measurement[43], ecological research for monitoring plant health[44], as well as numerous applications in medical care and environmental surveillance[45]. The reason behind this lag is attributed to the complexity and space requirements of current color sensing structures, which hinder their utilization in the aforementioned applications that prioritize device miniaturization.

To answer this question, according to reference[14], in this chapter, after being familiar with the characteristics of 2D materials and microfabrication technology, we will focus on the use of microfabrication to manufacture a micro color sensor based on 2D materials, which will be mainly used in the field of biomedicine, with their excellent optoelectronic performance and mechanical flexibility make them candidates for other uses.

## 4.1 Color Sensor

In order to mimic the visual capabilities of the human eye, a color sensor typically consists of three separate channels that respond to the red, green, and blue (RGB) components of incoming light, allowing for color determination based on these components. However, the design of these channels is limited by the availability of conventional semiconductors and the current fabrication technology used for planar devices. Typically, these channels are created by arranging a lateral array of identical photodetectors and placing color filters on top to separate the different color components. An example of this approach is the use of a silicon photodetector array coated with a Bayer color filter, as shown in Fig. 8. To achieve accurate color recognition, this structure requires at least four adjacent detectors (including two for the G-channel) to work together, leading to increased physical space requirements and the aforementioned challenges. While the Foveon sensor[46] uses a vertical color sensing configuration, it does not achieve the same level of color recognition accuracy as the Bayer structure[47], thus limiting its practical applications. Consequently, there is an urgent need for an alternative color sensing system that can address these challenges while maintaining a compact design and ensuring precise color detection. The recent progress in van der Waal semiconductors (vdW-Ss) and stacking

techniques[48-50] presents a promising alternative approach to overcome this dilemma by inspiring innovative hardware designs.

### 4.1.1  Conventional Color Sensor

The most common commercial color sensor is Bayer filter now days. The Bayer filter was invented in 1974 by Bryce Bayer, an employee of Eastman Kodak[51].The filters comprise of red, green, and blue (RGB) colors, with only one color per pixel. Each pixel is placed on a plane in parallel. This layout can ensure that any incident light can be accurately decomposed into different RGB components, but it is not suitable for the design of miniature sensors, because it takes up too much space and becomes an important obstacle on the way of miniaturization, as shown in Fig. 8. Although Foveon sensor has changed the traditional planar distribution and used a vertical stacking structure, it still cannot be widely used in bio sensors due to the use of silicone as a sensing material, which reduces its color sensing accuracy. Therefore, how to maintain high-accuracy RGB recognition while miniaturizing the size is the focus of our research in this chapter, and it is also an important link to promote the development of miniaturized color sensors in the field of biomedical monitoring.
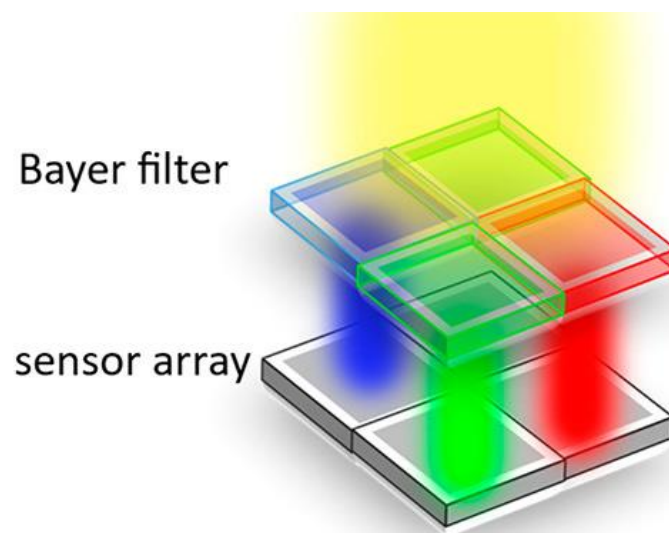


*Figure 4.1 Bayer filter.*

### *4.1.2    Miniatured Van Der Waals Semiconductor Color Sensor Fabrication*

Unlike other color sensor, we choose vdW-S material as the sensing layer material in this thesis. In comparison to conventional semiconductors, vdW-S offer a diverse array of options and the ability to finely tune their band structures. This characteristic allows us to utilize optimal materials for detecting red (R), green (G), and blue (B) light without the need for additional color filters. Additionally, thanks to the improved stacking methods[52, 53], we can fabricate sophisticated vertical optoelectronic architectures without any concerns such as lattice mismatch, Drawing inspiration from these distinct advantages, we present a compact and vertically oriented color sensor. By stacking layered materials with $CuIn_7Se_{11}$, InSe, and GaS, we have engineered separate R-, G-, and B-channels, as demonstrated in Fig. 9. The stacking order of RGB from bottom to top is determined according to the incident wavelength. Red light has the longest wavelength, so the R layer is at the bottom. However, such an orientation is irreversible, because if R is on the uppermost layer and B is on the lowermost layer, the blue light with the shortest wavelength has greater excitation energy, causing it to be simultaneously absorption by channel R and G on its path penetrate to B channel, which will seriously affect the accuracy of induction, so this stacking order is carefully considered.
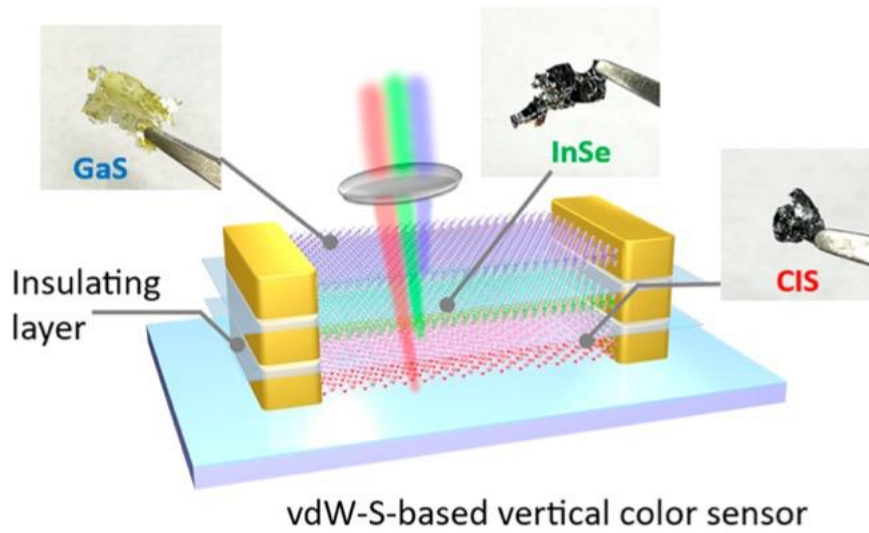
*Figure 4.2 vdW-S based vertical color sensor.*

To proceed with the implementation of the stacked vdW-S color sensor, our initial objective involves carefully selecting suitable materials from a comprehensive database. These materials must align with the principles outlined by the International Commission of Illumination (CIE) that govern color sensing[54, 55]. A color sensor fundamentally requires three distinct channels, each with maximum photoresponse in the RGB light spectrums, while also ensuring reasonable spectral overlaps, as illustrated in Fig. 10. In this structure, all sensing channels actively react to incident light and generate corresponding outputs, such as photocurrents. Color measurement is derived from the ratio of these outputs. However, excessive or insufficient spectral overlap can lead to inaccuracies in color recognition. Fig. 10b and Fig. 10c depict the inadequate discernment of light color due to these issues. Excessive spectral overlap poses a significant challenge for silicon-based Foveon sensors[56], as their narrow bandgap makes them equally sensitive to any incident light. Moreover, the wavelength-dependent penetration depths of these sensors fail to effectively separate these components. A similar problem may arise in vdW-Ss, especially in relation to the R-sensing material, where a narrower bandgap can intensify the

response to G- and B-light, resulting in excessive spectral overlaps. Similar concerns apply to the G-sensing material. Therefore, the crucial and initial step in realizing vdW-S color sensors is identifying materials with relatively narrow photoresponse spectra concentrated within the R-, G-, and B-ranges, while ensuring rational spectral overlaps.
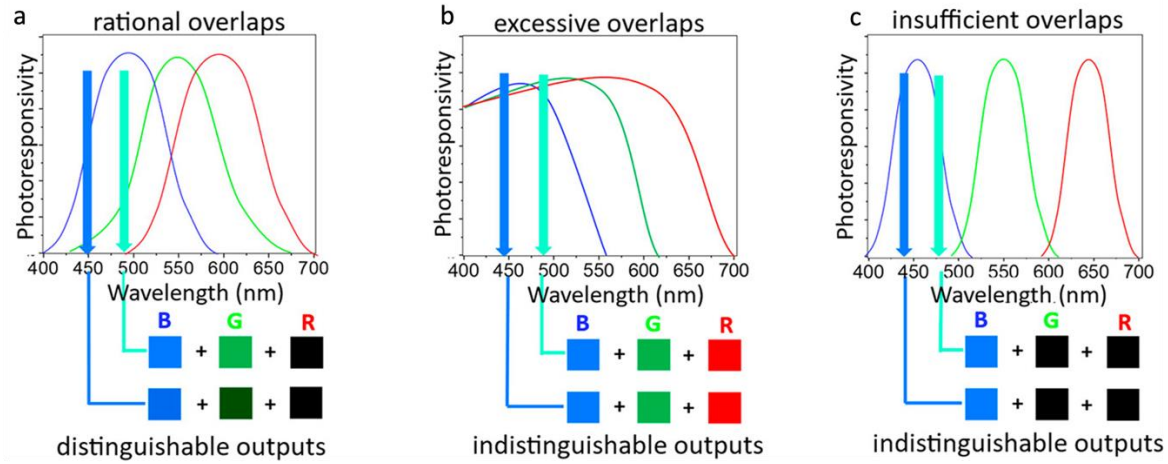


*Figure 4.3 Illustration of color sensing principle.*

For the blue sensing channel, we opt for GaS with a thickness of approximately 25 nm, primarily due to its relatively large bandgap[57]. Simultaneously, InSe is employed as the material for the green sensing channel, owing to its unique and intriguing band structure that offers an elegant solution to meet the requirement of spectral overlap. In comparison, the search for an appropriate red sensing vdW-S proves to be more challenging. We encounter difficulties in identifying a III-VI material that can replicate the intricate band structure mentioned earlier while possessing a narrower bandgap. Fortunately, our exploration leads us to discover layered $CuIn_7Se_{11}$ (CIS), a promising ternary vdW-S. It captures our attention as we find that CIS exhibits a stronger photoresponse in the 600-700 nm range and allows for controllable sensitivity in the G- and B-regions, making it an ideal candidate for the R-sensing channel.

With the material candidates identified, we proceed to fabricate a prototype stacking color sensor utilizing these vdW-Ss. The fabrication process involves employing mechanical exfoliation to isolate the vdW-Ss with the desired thicknesses from the bulk crystals. Subsequently, we perform a dry transfer method to construct the vertical color sensor prototype in a bottom-up approach, as illustrated in Fig. 11. In specific steps, we begin with a 10 nm layer of CIS as the R-sensing channel, located at the bottom of the entire stacking structure. Electrodes are patterned onto this layer using our custom-built direct laser writing system. Next, we introduce the first insulating layer, achieved through the deposition or transfer of dielectric materials like $MgF_2$ or mica. The dry transfer stage which built up by us is shown in Fig. 12. On top of this insulating layer, we repeat the same procedure to establish the G-sensing channel composed of a 13 nm layer of InSe. Lastly, we fabricate the B-channel on the uppermost layer using a 25 nm GaS layer. The insulating layer serves the dual purpose of isolating the vdW-Ss from exposure to the surrounding environment, thus significantly prolonging the device's lifespan in ambient conditions. Notably, throughout our month-long series of repeated tests, we observed no degradation in device performance.
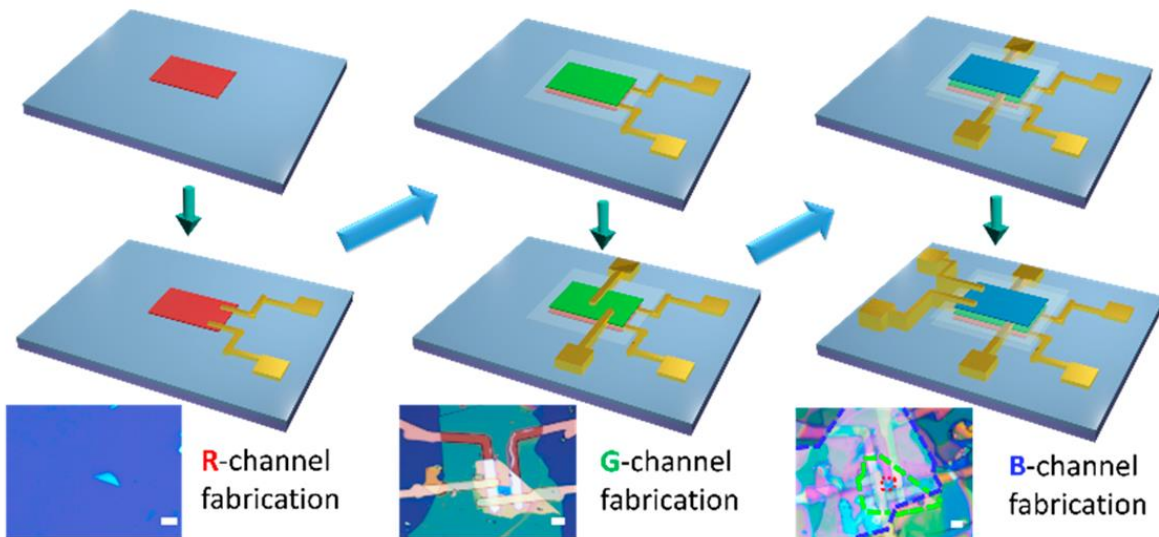


*Figure 4.4 vdW-S based color sensor device fabrication workflow.*
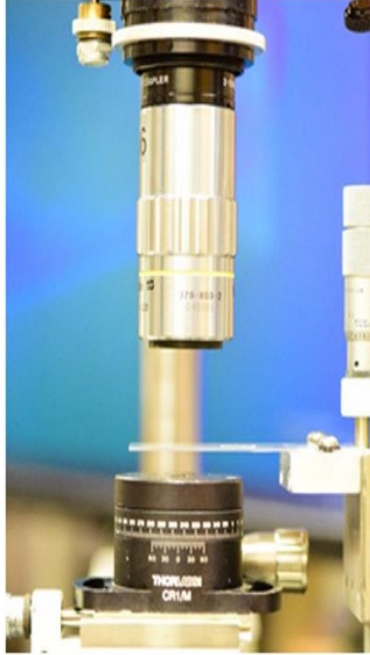
*Figure 4.5 Dry transfer stage.*

## 4.2   Performance and Application of Miniatured Color Sensor

### 4.2.1   *Photoelectric Characterization*

After completing the fabrication of the color sensor, we conducted a series of characterization tests to verify the correctness of its color sensing function. The first and most important test is the response spectrum of the three sensing layers to the corresponding colors. As we said above, the discrete sensing layer should only have a strong response to the only one color among RGB, but the spectral curves of these three should also have a reasonable overlapping area at the same time, otherwise it will not be possible to achieve accurate RGB sensing. Thanks to the three vdW-S materials we have chosen, we obtain the photoresponsivity (P.R.) spectra of the RGB sensing channels with a bias voltage of 1 V in Fig. 13. The photoresponse spectra (P.R.) of these RGB-channels calculated with the equation of $R(\lambda) = [I_{light}(\lambda) - I_{dark}]/P(\lambda)$.
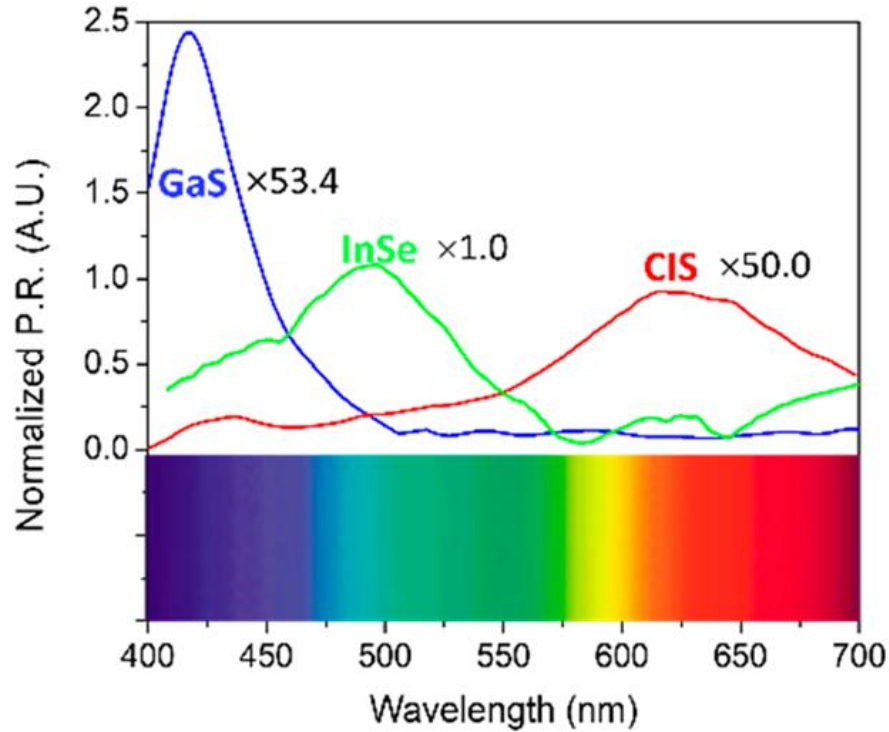
*Figure 4.6 Normalized photoresponsivity (P.R.) spectra of the RGB sensing channels with a bias voltage of 1 V.*

It is important to note that the spectrum has been normalized, signifying that based on the aforementioned formula, the red, green, and blue response values are multiplied by specific factors: 50.0, 1.0, and 53.4, respectively. This normalization process ensures that the regions covered by each spectral curve are balanced, enabling white light with a uniform spectrum to generate identical response levels across all channels (i.e., maintaining a 1:1:1 ratio). The process referred to as white-balance (WB) calibration is widely recognized and serves as a crucial stage in achieving precise color perception, as will be elaborated in the upcoming discussion. To provide visual aid, we include a spectral chart below the photo-response curves, effectively showcasing the successful execution of the intended functions by each sensing layer in our prototype. Specifically, the CIS component predominantly detects red light, InSe exhibits notable responsiveness to green color, and GaS operates within the blue spectrum. It is noteworthy that

these sensing layers intelligently overlap, aligning with their respective peaks as required by the fundamental principles of color sensing, ensuring accurate color identification. In addition, we added corresponding filters in the experimental measurement to weaken the influence of the light response in the UV and infrared regions, so the obtained spectral response is completely from the visible light region.

An important aspect to consider is the significant variation in photocurrent levels observed among these sensing layers. This variation arises due to our experimental setup, wherein we apply a uniform 1 V bias voltage to all sensing layers during spectrum acquisition and subsequent characterization. This simplified approach was adopted to facilitate discussion and ensure device protection throughout the investigation, without compromising the overall conclusions. However, it should be noted that such a uniform bias voltage is not necessary for practical applications. For instance, at the 1 V bias voltage, the photocurrent of the CIS layer is lower compared to that of InSe. Nonetheless, as depicted in Fig. 14, when a higher bias voltage is applied, the photocurrent of the CIS layer increases significantly and eventually matches that of the InSe layer. This behavior can be attributed to the improved collection efficiency of photogenerated charge carriers facilitated by a stronger electrical field.

In the case of the GaS layer, the low readings are influenced not only by the bias voltage but also by the substantial Schottky contact barrier. This challenge is commonly encountered in wide bandgap semiconductors like GaN[58]. As demonstrated in Fig. 14, the performance of the GaS layer can be notably enhanced by utilizing alternative contact materials with lower Schottky barriers and employing higher bias voltages. However, it is important to adjust the normalization factor for WB correction accordingly in such cases.
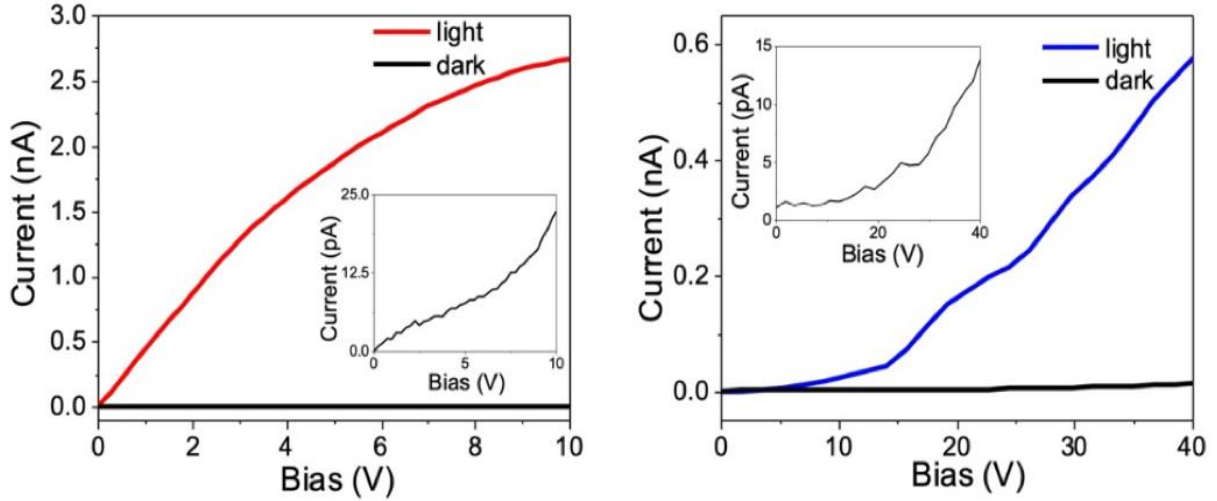
*Figure 4.7 Photocurrent and dark current curves of R(left)/B(right) sensing channels.*

In addition to spectral response, another vital requirement for accurate color sensing is the linear relationship between photocurrent and incident light power within each sensing channel. This linear dependency is crucial because color measurement relies on the relative ratios of photocurrent readings from these channels, rather than their absolute values that solely indicate light brightness. Therefore, maintaining excellent linearity in each channel is essential to ensure precise color measurements that remain unaffected by changes in intensity. Without this linearity, the detected light color may shift or fluctuate as the intensity of the incident light changes. In order to achieve it, we further tested the photocurrent-power (I-P) dependence of the GaS, InSe, and CIS layers. To assess the photocurrent-power (I-P) dependence tests, we conducted experiments where we illuminated them with lasers emitting at 458 nm(Blue), 514 nm(Green), and 647 nm(Red), respectively. The excitation intensity was adjustable across three orders of magnitude, as illustrated in Fig. 15. Remarkably, all three layers exhibited exceptional linearity within this broad intensity range, highlighting the color sensor's linear dynamic range (LDR) of at least 66 dB. The LDR is defined as $20 \times \log10\ I_{max}/I_{min}$, where $I_{max}$ and $I_{min}$ represent the highest and lowest

excitation power values in Fig. 15. It should be noted that this linear relationship will determine that no matter how the intensity of the incident laser changes, the RGB sensing values of the three channels will follow the same linear change, which means that the value of white balance calibration(53.4, 1.0, 50.0) will not change. Thus demonstrating the consistency of this correction. It is worth mentioning that no photocurrent saturation was observed during our experiment, suggesting that the actual LDR of our device exceeds this calculated value. Additionally, we examined the dark current and photocurrent I-V curves for each sensing channel, as depicted in Fig. 16. The GaS, InSe, and CIS layers were excited by lasers at 458 nm, 514 nm, and 647 nm, respectively, with an intensity of 17.5 mW/cm². We confirmed very low and consistent dark currents across all sensing channels. Furthermore, the photocurrents increased as the bias voltage was raised, indicating that employing a higher voltage within a reasonable range, without saturating the sensing layers, can enhance their sensitivity and detectivity. The IV curve that is not linear and perfect actually reflects the contact problem of the device electrode, and the Schottky junction is an important reason that affects its performance. Especially for B-channel materials GaS, its wide bandgap makes it difficult to find a suitable electrode contact material, which is why its detectivity (external quantum efficiency) is not high enough. Although the current setup is adequate for demonstrate miniature color sensor performance, this situation may be improved by optimizing the electrode metal material, which is also the focus of our follow-up research.
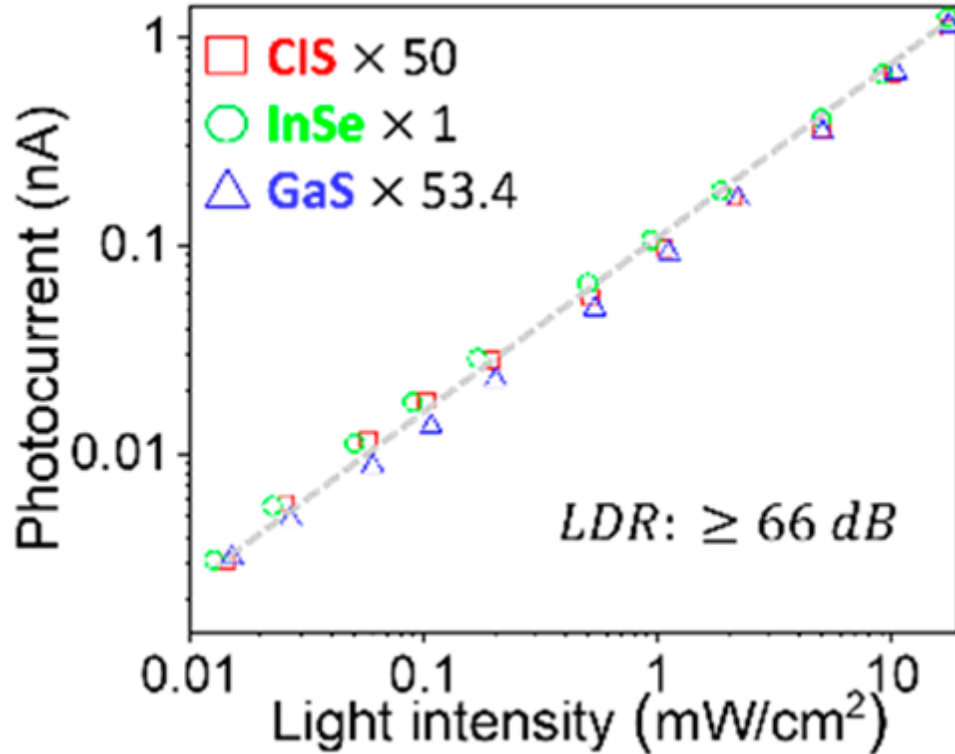
*Figure 4.8 Photocurrent−light intensity curves of each sensing channel measured with a bias voltage of 1 V.*
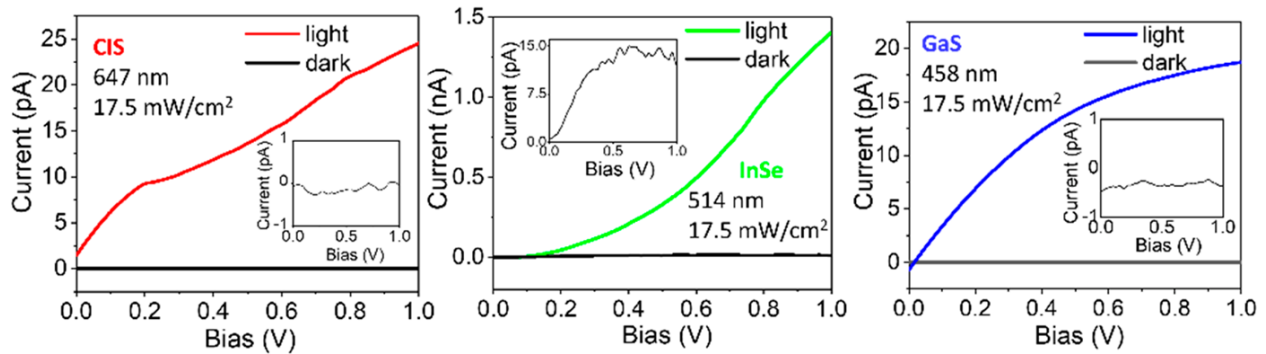


*Figure 4.9 Photocurrent and dark current curves of the RGB sensing channels excited with 17.5 mW/cm2 and 647, 514, and 458 nm laser, respectively. Insets show the detailed data of the dark currents.*

### 4.2.2   Color Sensing Principle

The comprehensive optoelectronic characterizations described above, particularly the

photocurrent spectrum and I-P measurements, have laid the groundwork for the subsequent

investigation into the color sensing capabilities of the device. With these characterizations

completed, we can now proceed to utilize this color sensor for the actual detection of RGB lights. The color temperature, is a crucial parameter for various applications such as metallurgical process control[59] and star activity monitoring[60]. In our experiment, we illuminated the sensor using a halogen lamp, as depicted in Fig. 17. By adjusting the power supplied to the lamp, we were able to manipulate the filament temperature, which closely corresponds to the color temperature being measured. This approximation is possible because the incandescent tungsten wire behaves as an approximate blackbody radiator. The color captured by our prototype device was represented as (R, G, B), indicating the photocurrent readings from each sensing layer. The specific readings are provided in the upper table of Fig. 18
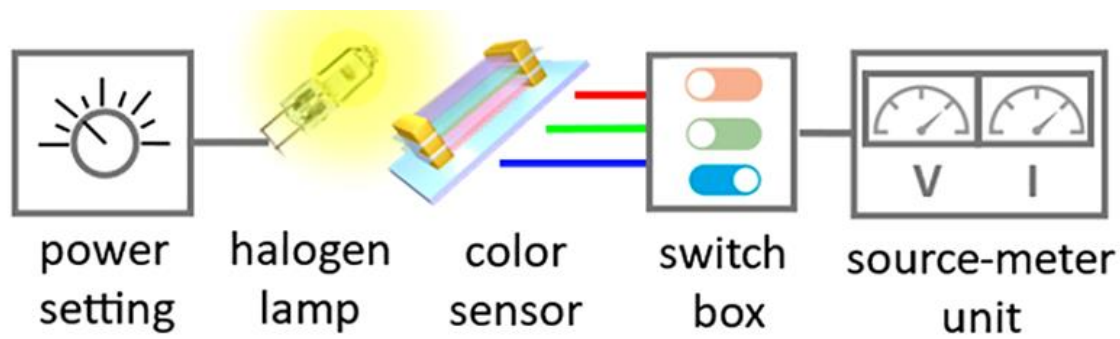


*Figure 4.10 Halogen lamp experimental setup for the color temperature measurement experiment.*

## RGB Raw Values

|          | S1    | S2    | S3    | S4    |
|----------|-------|-------|-------|-------|
| CIS (pA) | 84.0  | 135.0 | 184.0 | 233.0 |
| InSe (nA)| 3.59  | 6.21  | 7.66  | 10.89 |
| GaS (pA) | 4.60  | 11.9  | 24.8  | 38.5  |

$M_{WB}$

## Corrected Tristimulus Values

|      | S1   | S2   | S3   | S4    |
|------|------|------|------|-------|
| CIS  | 4.20 | 6.75 | 9.20 | 11.65 |
| InSe | 3.59 | 6.21 | 7.66 | 10.89 |
| GaS  | 0.25 | 0.64 | 1.32 | 2.06  |

*Figure 4.11 The RGB raw values (upper) sensed by our device under four different power setting points (S1−S4) and the corrected tristimulus values (lower) calculated with the color correction matrix.*

However, like other color sensors, the obtained color values (R, G, B) are influenced by the physical characteristics, particularly the photo-response spectra of the device. Therefore, it is necessary to convert the raw color values into a standardized and device-independent format for data exchange and further processing. The CIE 1931 XYZ color space is widely accepted as a color representation system for this purpose. To obtain the standardized values in the CIE system, we must first map the raw color coordinates to the CIE color values of (X, Y, Z), which can be calculated using specific formulas.

The CIE color correction matrix (CCM), denoted as M, is a 3x3 matrix that plays a crucial role in the conversion process. Determining the CCM involves several steps, including white-balance correction, color-space transformation, and more. Each step requires its corresponding correction matrix, such as $M_{WB}$ for white-balance correction and $M_{CT}$ for color-space

transformation. The final CCM is obtained by multiplying these matrices, expressed as $M = M_{CT} \times M_{WB}$.

$$\begin{pmatrix} X \\ Y \\ Z \end{pmatrix} = M \cdot \begin{pmatrix} R \\ G \\ B \end{pmatrix}$$

In the case of our prototype sensor, the photoresponse spectra exhibit distinct peaks for red (R), green (G), and blue (B) channels, and they demonstrate appropriate spectral overlap akin to the standard tristimulus curves (depicted in Fig. 19). Based on this observation, we can hypothesize that $M_{CT}$ approximates an identity matrix, indicating that $M \approx M_{WB}$.

$$M_{WB} = \begin{pmatrix} 50.0 & 0.0 & 0.0 \\ 0.0 & 1.0 & 0.0 \\ 0.0 & 0.0 & 53.4 \end{pmatrix}$$
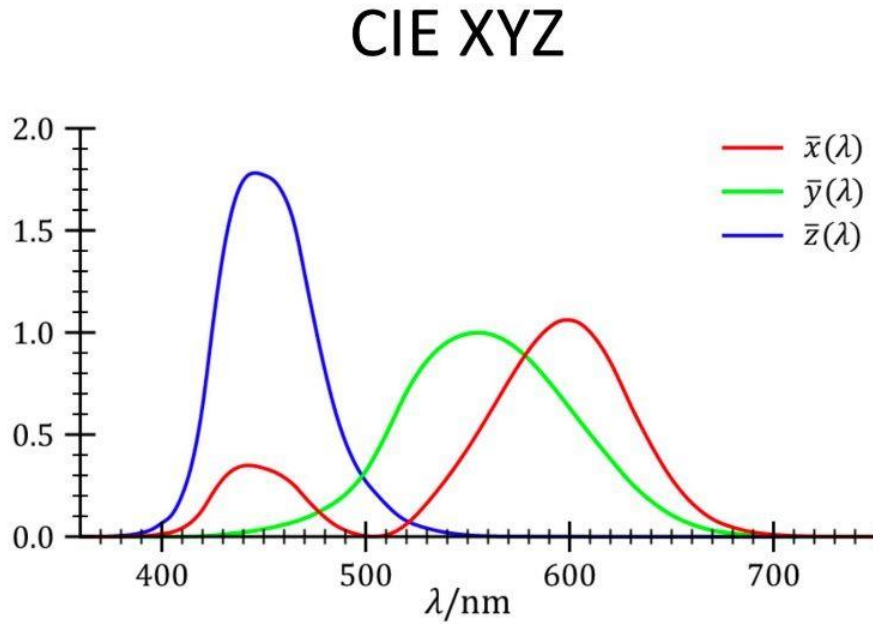


*Figure 4.12 Tristimulus curves.*

The matrix elements mentioned are the normalization parameters that ensure equalization of the spectral areas for the CIS, InSe, and GaS layers. Consequently, the lower table in Fig. 18 displays the calculated XYZ values corresponding to the four power setting points (S1-S4). While

this is an initial approximation, it is evident that even at this stage, our prototype sensor exhibits a reasonable level of accuracy in color sensing. Furthermore, the three-dimensional representation (X, Y, Z) can be simplified into a two-dimensional form using the appropriate formula.

$$a = \frac{X}{(X + Y + Z)}$$

$$b = \frac{Y}{(X + Y + Z)}$$

### 4.2.3   Color Sensing Characterization

The simplified representation of the color in a two-dimensional form is achieved by using the formula that disregards the absolute light intensity. In this representation, only the ratio among the coordinates, rather than their absolute values, signifies the light color. These values, denoted as (a, b), serve as the color coordinates within the well-known two-dimensional CIE 1931 color space[61], as illustrated in Fig. 20. The four power setting points are labeled, and the white spots on the figure represent the respective color temperatures of 2500 K, 2750 K, 3000 K, and 3400 K. To assess the accuracy of our color sensing capabilities, we determined the color temperatures of additional points, specifically 2650 K, 2830 K, 2960 K, and 3250 K. This was accomplished by fitting the emission spectra of these specific settings with blackbody radiation curves, as illustrated in Fig. 21. It is important to note that, due to the use of a silicon photodetector for spectrum collection, only the spectra within the UV to visible light range (400-800 nm) were utilized for the fitting process. Upon comparison, we found a close correspondence between the datasets obtained from the two aforementioned methods, with an error margin of less than 5.0%. This solidifies the practical feasibility and measurement accuracy of our device architecture, providing strong evidence of its reliable performance. Our sensor successfully distinguished these colors, although

there were some deviations between the measured and expected coordinates. This can be attributed to the fact that our process only included white-balance correction (WB), while the introduction of $M_{CT}$ could result in more precise measurements[62, 63]. However, calibrating MCT requires sophisticated and well-established procedures, which are beyond the scope of this study that primarily focuses on demonstrating fundamental principles and practical application potentials.
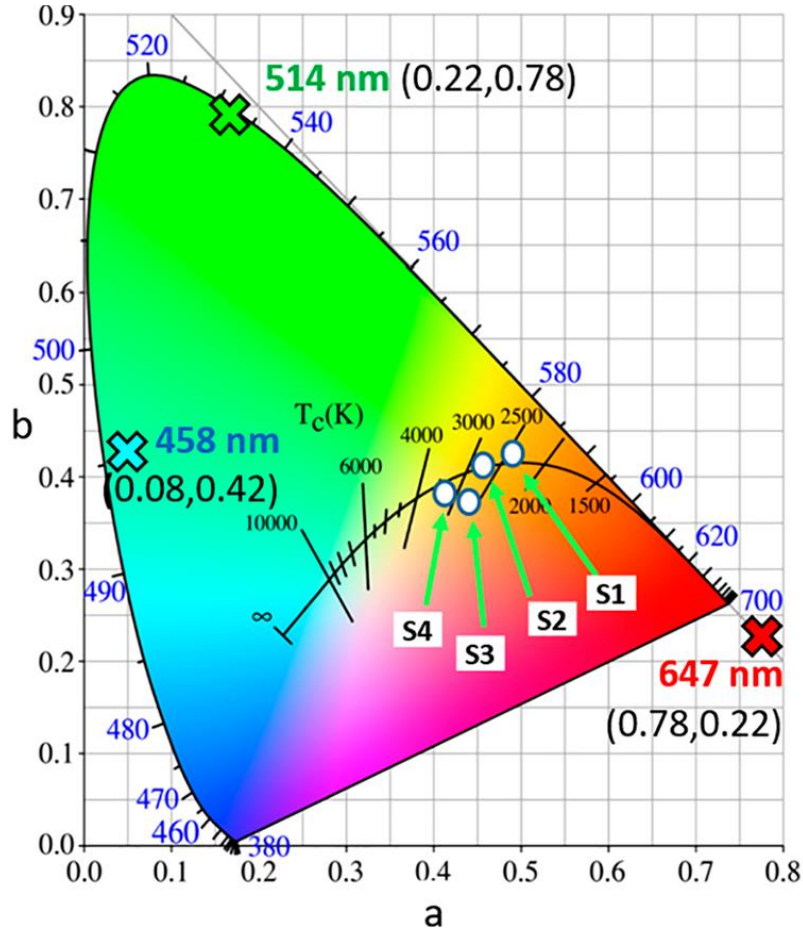


*Figure 4.13 CIE color space chart with the experimentally measured color coordinates of the halogen lamp on S1−S4 setting points (marked with solid white circles).*
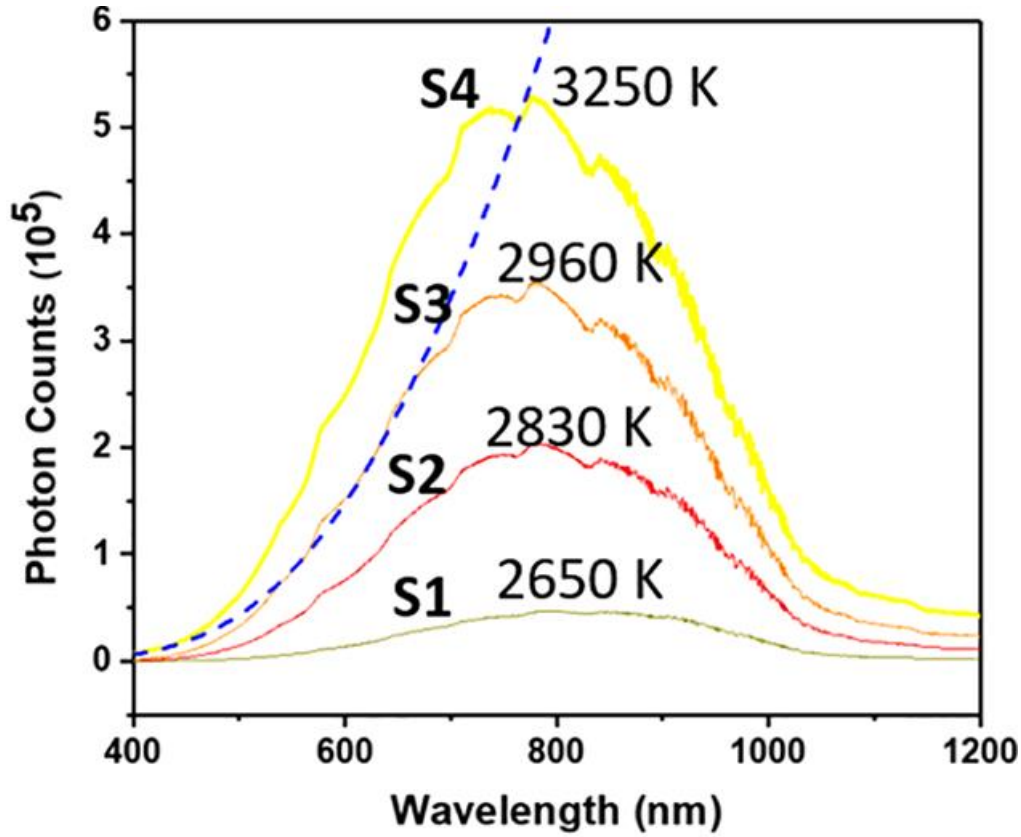
*Figure 4.14 Black body radiation curves.*

Furthermore, Fig. 22 provides the time response curve for each sensing channel, aiming to characterize the dynamic performance of our color sensor. These measurements contribute to a comprehensive understanding of the sensor's capabilities beyond its static behavior.
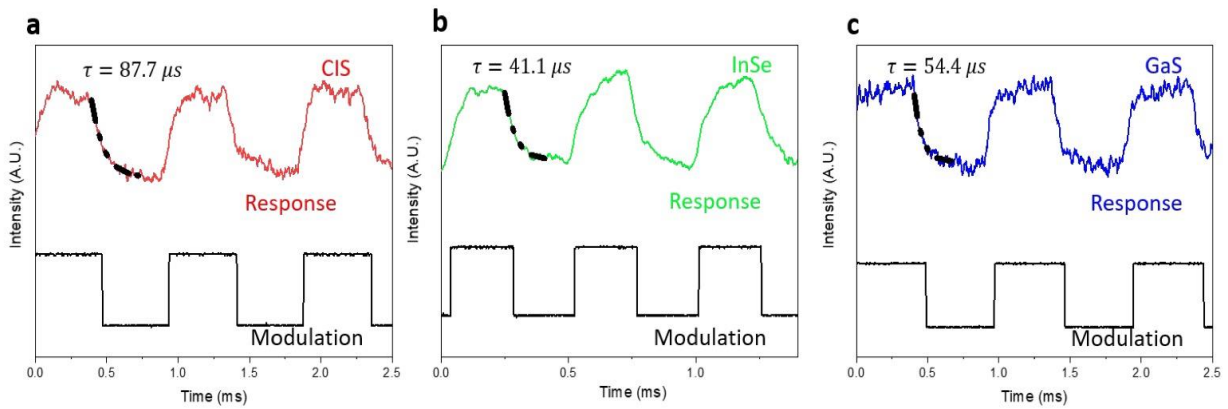


*Figure 4.15 The response time of each sensing layer.*

**4.3    Scalability of Van Der Waals Semiconductor Miniatured Color Sensor**

*4.3.1    Scalability Design and Fabrication*

In addition to functioning as an independent color recognition unit, our innovative design can be seamlessly integrated into arrays or matrices, making it an ideal solution for vision devices in various fields. The compact nature and impressive optoelectronic capabilities of our architecture enable us to meet the growing demand for smaller and more efficient devices, aligning with the latest advancements in microrobotic techniques and their applications in biology and the environment[64-67]. To achieve this, we devised a circuit diagram (Fig. 23) for a three-pixel color sensor array, comprising a total of nine photodetectors, each equipped with two electrodes (top and bottom). By connecting the top electrodes within the same channel and bundling all three bottom electrodes within each pixel, we obtained channel selection (CS) terminals and pixel selection (PS) terminals, respectively. This configuration grants us precise control over individual channels and pixels by combining different CS and PS terminals. To realize this three-pixel sensor array, we followed a workflow (Fig. 24) similar to the transfer and stacking procedure discussed earlier. The resulting monolithic structure was then divided into three distinct pixels using a focused ion beam (FIB), ultimately yielding the desired three-pixel color sensor array. A fabricated SEM image (Fig. 25) showcases the structure, providing visual evidence of the potential and feasibility for scaling up our device architecture. As the availability of wafer-scale InSe[68] and other van der Waals semiconductors (vdW-Ss)[69-71]expands, we can readily fabricate scalable image sensors that incorporate our color recognition mechanism.
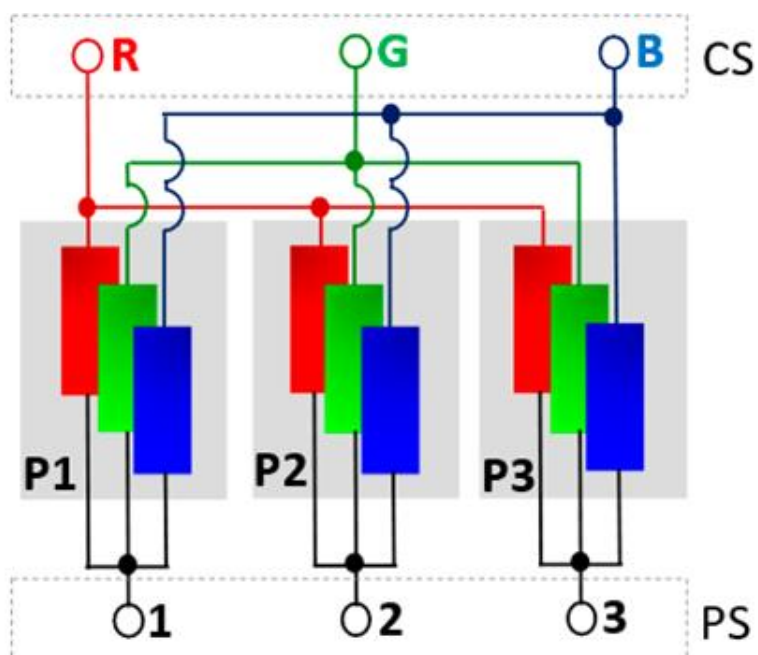
*Figure 4.16 Circuit of three-pixel color sensor array.*
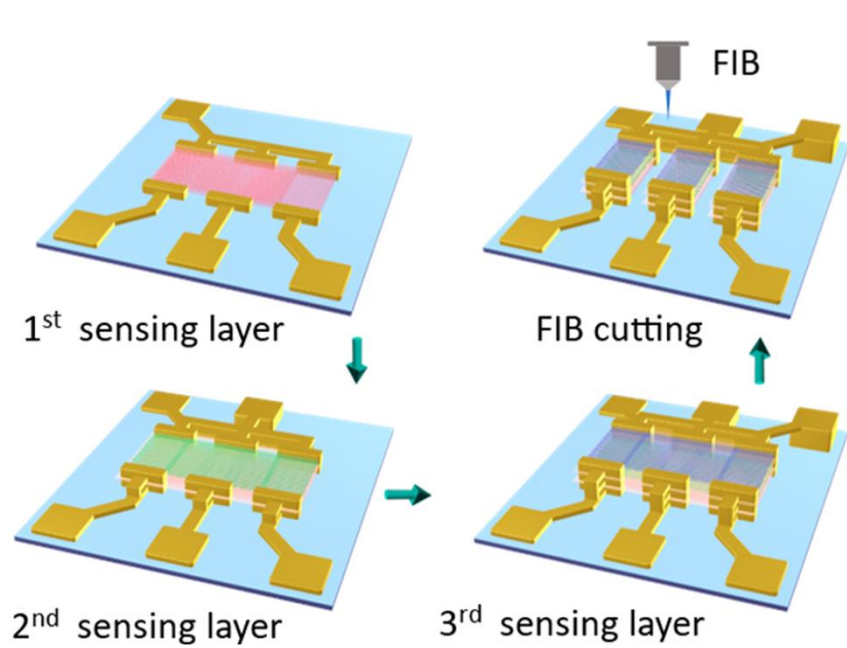


*Figure 4.17 Device fabrication workflow of three-pixel color sensor array.*
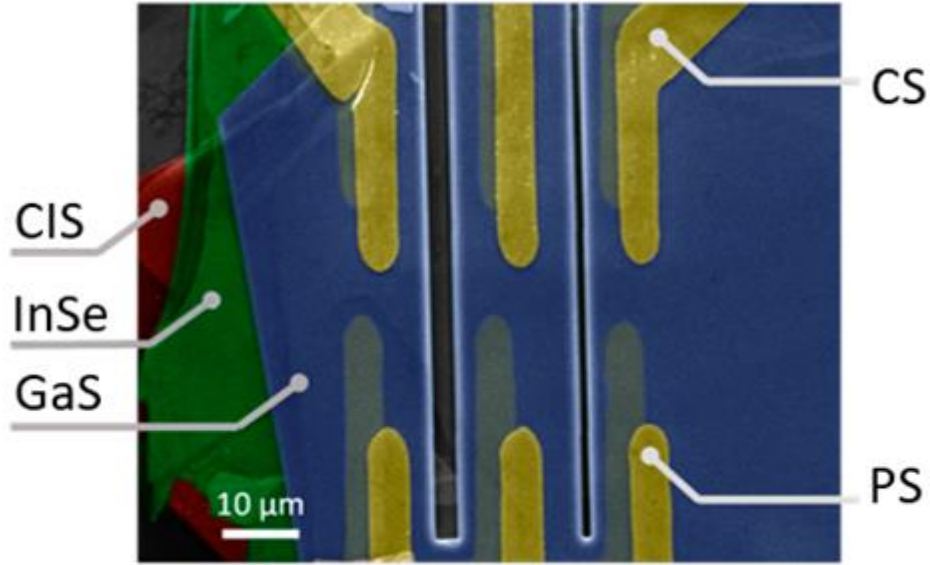
*Figure 4.18 Fake-color SEM image of three-pixels vdW-S-based vertical color.*

### 4.3.2 Photoelectric and Color Sensing Characterization

Upon completing the fabrication, we proceeded to conduct two vital tests to evaluate the functionality of the device: the spatial resolution of light intensity distribution and color recognition. For the spatial resolution test, we employed a custom-made probe station and directed incident light onto the device using a 20 μm diameter optical fiber. Precise control of the optical fiber's position was achieved through a micromanipulator, enabling targeted illumination of individual pixels. Fig. 26 showcases the experimental setup, encompassing the device under investigation, electrical probes, and the optical fiber. The illuminated spot in the image represents the light projected onto the sample. By systematically moving the optical fiber from the left to the right of the array, we obtained a mapping of the photocurrents (G-channel), as depicted in Fig. 27. This mapping unequivocally validates the device's ability to detect and spatially resolve the distribution of light intensity. Additionally, we assessed the color recognition capability by introducing R (red), G (green), and B (blue) lights to the first, second, and third pixels, respectively.

Fig. 28 presents the responses from these pixels in the form of colored grayscale, unequivocally demonstrating their accurate color recognition. This successful demonstration of spatially resolved color recognition underscores the immense potential of our device architecture for future applications, wherein ultracompact image sensors can be realized through the seamless integration of multiple pixels at a large scale.
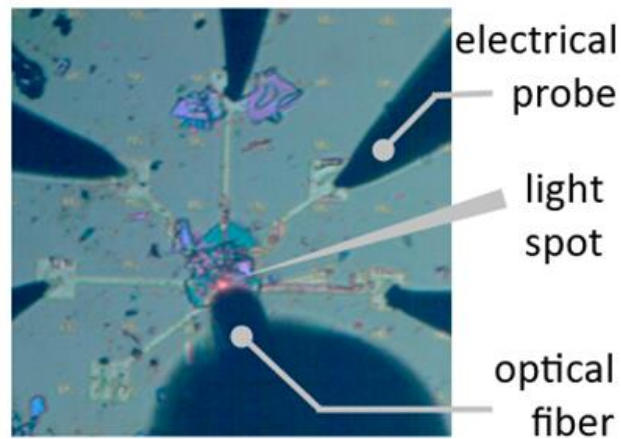


*Figure 4.19 The optical image of experiential configuration for the spatial resolved light intensity mapping and color sensing.*
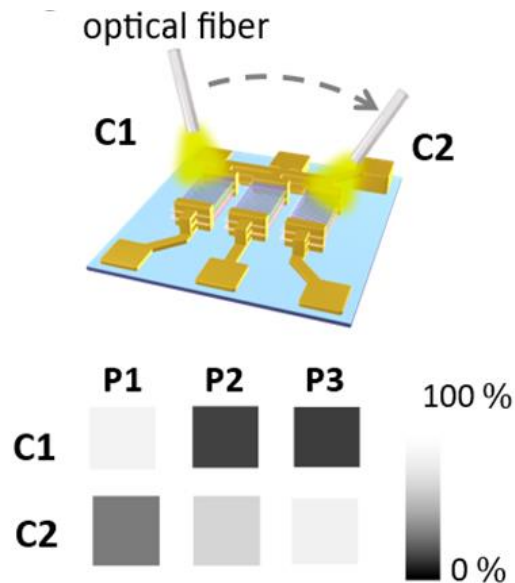


*Figure 4.20 Detection of the light intensity distribution.*
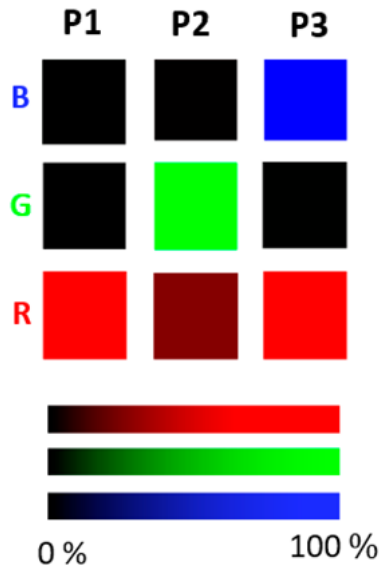
*Figure 4.21 RGB light color recognition test on the three-pixel color sensor array.*

It is worth mentioning that the above-mentioned light intensity distribution characterization is done in a vacuum chamber (Fig. 29). This is to avoid unnecessary external disturbances. This is a home-made vacuum chamber. Its vacuum degree reaches $10^{-9}$ Torr, and the temperature can be controlled from room temperature to 5k, which greatly ensures the comprehensiveness of the test.
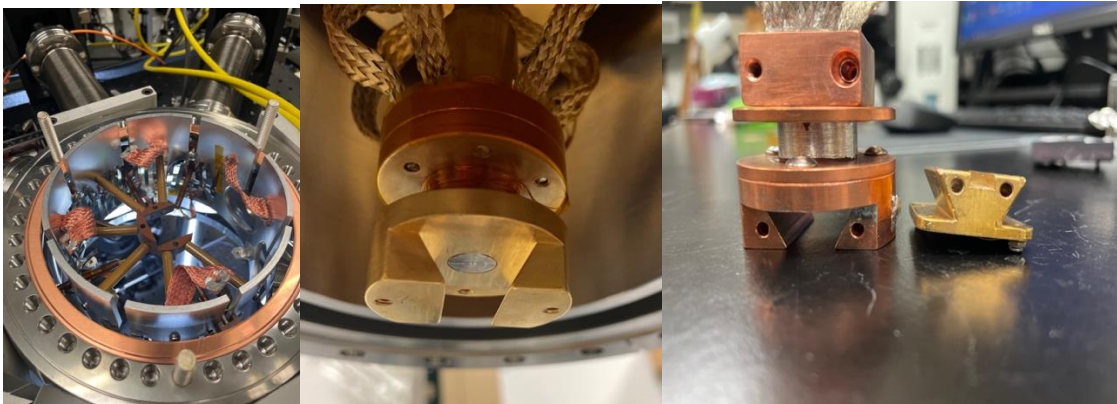


*Figure 4.22 Vacuum chamber and sample holder.*

Through the successful demonstration of a prototype color sensor utilizing vertically stacked van der Waals semiconductors (vdW-Ss), we have provided compelling evidence of the vast selection and versatile tunability of energy band structures within vdW-S materials. Expanding on this achievement, we employed microfabrication technology to implement an exceptional photoresponse in a stacked sensor configuration consisting of Copper Indium Sulfide (CIS), Indium Selenide (InSe), and Gallium Sulfide (GaS). This advanced sensor effectively senses the three primary colors of red (R), green (G), and blue (B), exemplifying its remarkable capabilities.

## 4.4 Spectrometer

### 4.4.1 Conventional Spectrometer

The spectrum has its origins in the 17th century, particularly with the pioneering work of physicist Isaac Newton in 1666[72]. Newton conducted the first-ever dispersion experiment of light, which involved directing a beam of sunlight into a dark room and allowing it to pass through a prism[73]. On the self-screen positioned behind the prism, he observed the scattering of light into seven distinct colors, resembling a rainbow. This phenomenon came to be known as spectroscopy. However, despite its significance, Newton's experiment on the spectrum received relatively little attention at the time. Over the course of more than a century, the study of the spectrum underwent significant development, exploration, and research. In 1859, Kirchhoff and Bunsen designed and constructed a spectroscopic device of exceptional quality for analyzing the spectrum of metals[74]. This device marked the world's first practical instrument for spectroscopy. Through the observation of spectral lines produced by various metals in flames and electric sparks, this device laid the initial groundwork for spectral analysis.

It was not until 1882 that Roland invented the concave grating[75], which involved directly engraving scratches onto a concave spherical surface. The concave grating served as a highly efficient integrated component within the imaging system of optical instruments, addressing the formidable challenges faced by prism spectrometers at the time. The introduction of the concave grating not only simplified the structure of spectroscopic instruments but also enhanced their performance significantly.

A spectrometer is an instrument that uses optical spectrum analysis technology to measure the wavelength or frequency of a substance to study its spectral characteristics[76]. It is widely used in physics, chemistry, geology, biology, medicine and other fields[77-83]. Spectrometers are mainly based on the analysis of spectral phenomena and the processes of absorption, scattering, and emission of atomic and molecular structure changes under the action of electromagnetic waves. A typical spectrometer includes components such as incident light source, sample chamber (or sample stage), dispersive element, detector, and data analysis device[84], as shown in Fig. 30. Wherein the dispersion element may be a prism, a grating or other diffractive elements. Accordi`ng to the experimental objects and fields of use, spectrometers can be roughly divided into various types such as ultraviolet-visible spectrometers, infrared spectrometers, mass spectrometers, and nuclear magnetic resonance spectrometers.
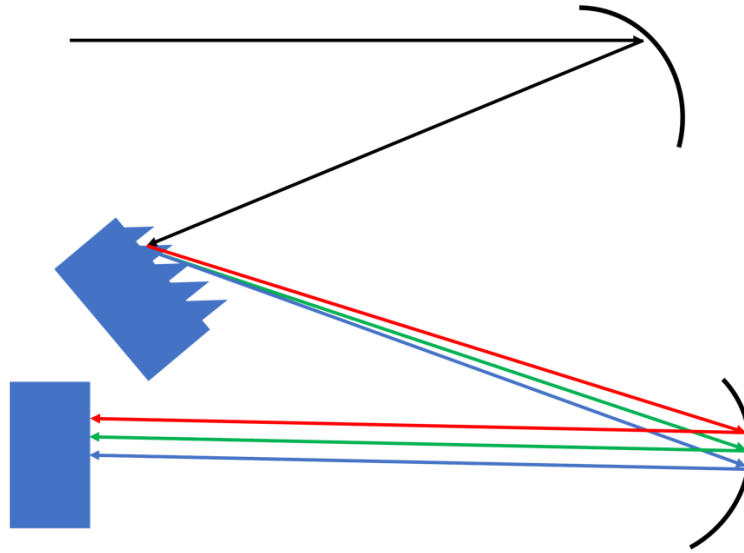
*Figure 4.23 Conventional spectrometer design.*

### 4.4.2   Miniature Spectrometer

Traditional bench-top laboratory spectrometers can provide unparalleled ultra-fine resolution and wide spectral range, but their structures are complex and bulky. In recent years, due to the rapid growth of the application space of spectral analysis, the miniaturization of spectrometers has attracted widespread attention due to the need for size reduction, cost reduction, and power consumption of portable and integrated spectrometers prior to the need for performance improvement. The development of micro-spectrometers mainly depends on the progress of micro-nano manufacturing technology and the improvement of computing power.

2D materials offer a diverse range and customizable band gaps, making them highly promising as photosensitive materials for various wavelengths. In this section, we utilize GaS and GaSe synthesized materials in varying proportions as the photosensitive layer. By employing microfabrication techniques, we vertically stack nine different composites, enabling wavelength detection within the visible light spectrum and achieving miniaturization of the spectrometer.

Nine different photosensitive layer materials are synthesized according to different ratios of GaS and GaSe, which are shown in Fig. 31.



*Figure 4.24 Different ratios of GaS and GaSe.*

We take the 1:9 synthesis as an example to introduce the specific synthesis process. First, we need to synthesize GaS, which requires Ga and S to be weighed according to the molar mass ratio of 1:1, and then fired in a furnace to complete the synthesis. The specific firing process is shown in Fig. 32.
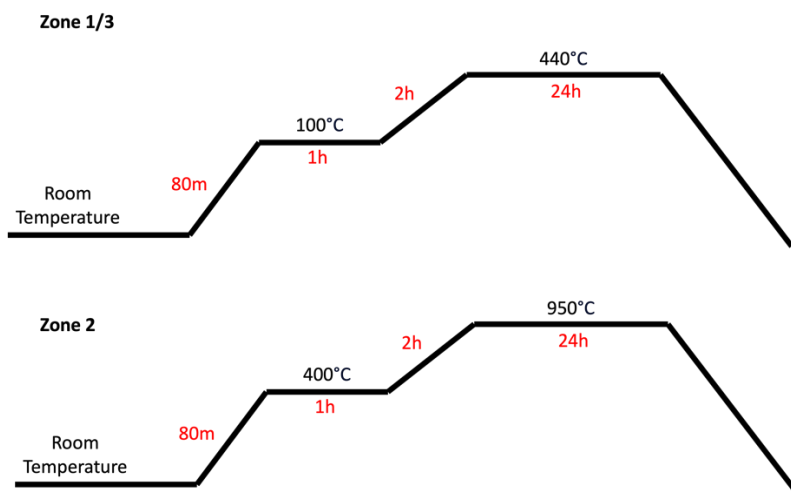


*Figure 4.25 GaS synthesis process.*

After obtaining enough GaS, we need to weigh GaS and GaSe respectively according to the molar mass of 1:9, and then complete the synthesis through furnace firing[85, 86]. For the other

eight kinds of materials, we only need to change the weighing weight in proportion, and then follow the same firing process to obtain the corresponding synthetic materials, which are the basis for making micro-spectrometers.

In order to break through the volume limitation of traditional spectrometers, we choose to stack the above nine materials in the vertical direction. Such a structure can greatly reduce volume consumption. The schematic diagram of the micro-spectrometer is shown in Fig. 33. Nine kinds of composites are stacked from bottom to top in order of corresponding response wavelengths from long to short. Layers are separated by insulating materials to prevent short circuits. Transparent insulating layers will not have any negative impact on incident light detection.
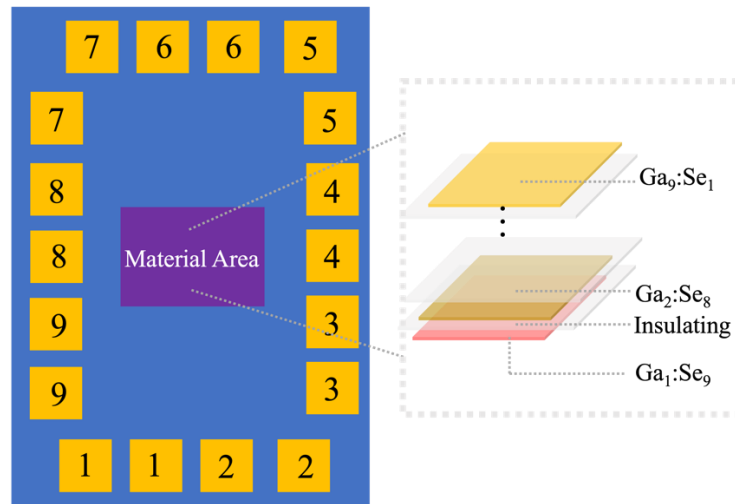


*Figure 4.26 Micro-spectrometer design.*

The design principle of this micro spectrometer may appear deceptively simple, yet its implementation necessitates an exceptionally high level of precision and expertise in micro device fabrication. The fabrication process involves meticulously stacking a total of 17 layers, each serving a specific purpose, including the insulating layer material. In our approach, we have carefully chosen the dry transfer method for stacking the 2D materials. This method offers numerous advantages over the wet transfer technique, most notably in providing a pristine and

uncontaminated surface[87, 88]. By employing the dry transfer method, we can create a cleaner plane, minimizing the presence of impurities and imperfections that could adversely affect the performance and reliability of the micro spectrometer. This is particularly crucial in the realm of micro device fabrication, where even the smallest irregularity or contamination can have significant repercussions on the overall functionality and accuracy of the spectrometer.

The meticulous process of stacking the 2D materials through dry transfer involves delicately manipulating and aligning each layer to ensure precise positioning and alignment. This level of precision is paramount in guaranteeing optimal light absorption, efficient wavelength detection, and accurate spectral analysis within the visible light spectrum. Furthermore, the utilization of the dry transfer method offers additional benefits in terms of process control and repeatability. It allows for enhanced reproducibility and consistency in the fabrication of micro spectrometers, enabling the production of high-quality devices with uniform performance characteristics.

In summary, while the design principle of a micro spectrometer may not be overly complex, the micro device fabrication process demands meticulous attention to detail and adherence to stringent manufacturing standards. By adopting the dry transfer method for stacking the 2D materials, we can ensure a pristine surface, free from impurities, and achieve the highest level of precision necessary for the successful development of a miniature yet powerful spectrometer. In order to ensure that the contact surface is clean, and the device performs well, we use the process shown in Fig. 34 to complete the micro fabrication of each layer.
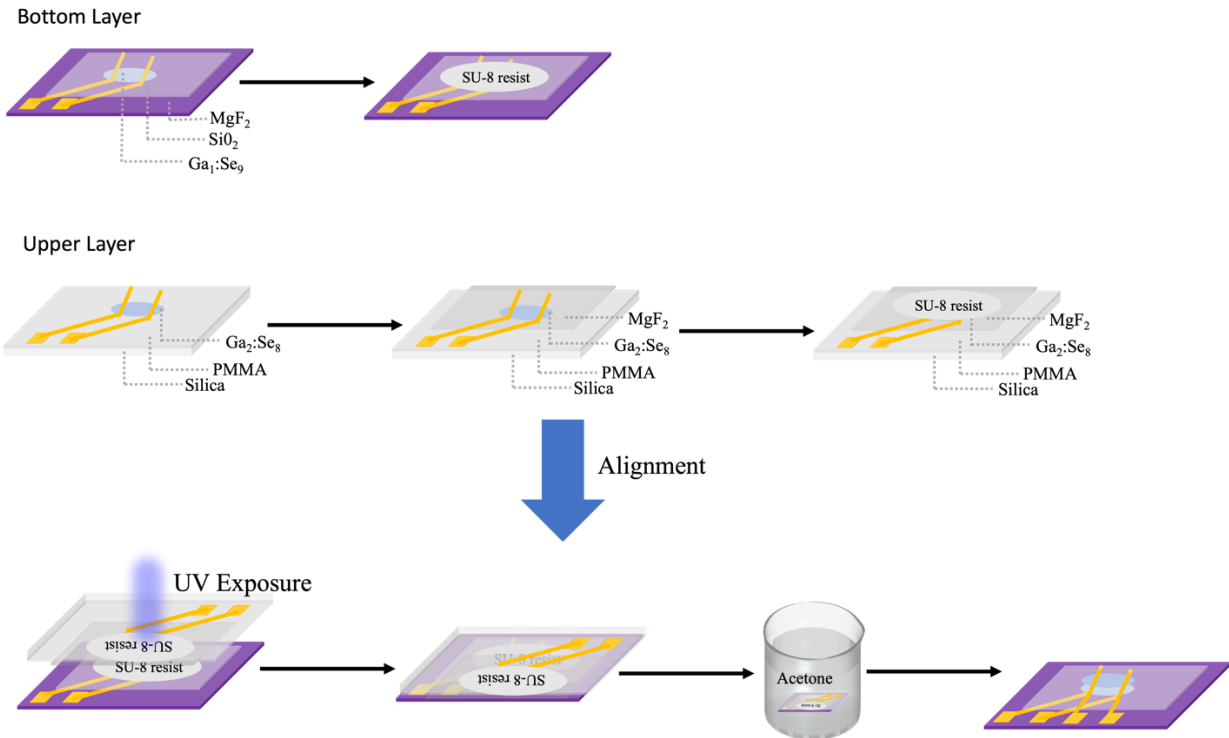
*Figure 4.27 Micro spectrometer fabrication workflow.*

Since the research focus of this thesis is on the exploration of the processing of micro-devices made of 2D materials, no more descriptions will be made on the subsequent specific applications and characterizations. However, the design and micro-processing scheme of the micro-spectrometer proposed based on the above process will help to overcome the difficulties in the manufacture of the micro-spectrometer: (1) the guarantee of the response range; (2) and the success of micro device manufacturing.

# 5    CHAPTER 5 STRAIN ENGINEERING OF VAN DER WAALS MATERIAL

In the first, second, and third chapters, we have conducted a comprehensive exploration of the optoelectronic properties of 2D materials, delved into the advancements in micro fabrication technology, and examined successful case studies of utilizing the latter to manufacture micro devices based on the former. However, beyond their exceptional photoelectric properties, 2D materials also possess remarkable mechanical properties, particularly flexibility and bendability[89, 90], which surpass those of conventional semiconductor materials. This outstanding flexibility positions 2D materials as highly promising candidates in the field of wearable devices[91, 92]. Furthermore, the fourth chapter delves into the implications of harnessing the mechanical flexibility of 2D materials in various emerging fields. Biomedicine, for instance, stands to gain significant advantages from the integration of flexible micro devices based on 2D materials. These devices can conform to the body's contours, enabling comfortable and non-invasive monitoring of vital signs, drug delivery systems, and implantable sensors.

In the realm of environmental monitoring, the flexibility of 2D materials can be leveraged to create compact and unobtrusive sensing devices. These devices can be deployed in various environmental conditions and conform to irregular surfaces, facilitating accurate data collection and analysis. The integration of two-dimensional materials' mechanical flexibility in artificial intelligence (AI) applications holds tremendous potential as well[93, 94]. Flexible micro devices based on these materials can enable the development of lightweight, portable, and energy-efficient AI systems. These systems can be seamlessly integrated into everyday objects, wearable devices, or even autonomous robots, paving the way for a new generation of intelligent and adaptive technologies.

In the fourth chapter, we delve into the challenges and opportunities associated with harnessing the mechanical flexibility of 2D materials for the development of micro devices. We explore novel fabrication techniques, innovative device designs, and potential applications in various industries. By unlocking the full potential of 2D materials' mechanical properties, we aim to pave the way for the creation of highly functional and versatile micro devices that push the boundaries of current technological capabilities.

## 5.1    Van Der Waals Semiconductor on Flexible Substrate

As discussed in the first chapter, 2D materials can be obtained from their bulk crystals through a process known as mechanical exfoliation. However, it is important to note that only monolayer or multiple layer flakes exhibit exceptional optoelectronic properties. Therefore, the thickness of the material plays a crucial role in micro device fabrication. Extensive research has been conducted to explore methods of obtaining larger areas of 2D materials while ensuring that the flakes are sufficiently thin, ideally consisting of a single layer. Although this section will not delve extensively into these techniques, it acknowledges the significant efforts invested in achieving larger and thinner 2D material flakes to enhance their suitability for micro device applications[95, 96].

The utilization of the remarkable mechanical flexibility of ultra-thin 2D materials is often achieved by constructing devices on flexible substrates. As depicted in Fig. 35[97], the manufacturing process involves employing a flexible base to support and accommodate the 2D material. Among the commonly used flexible substrates, polymers, such as polydimethylsiloxane

(PDMS), have garnered significant attention.
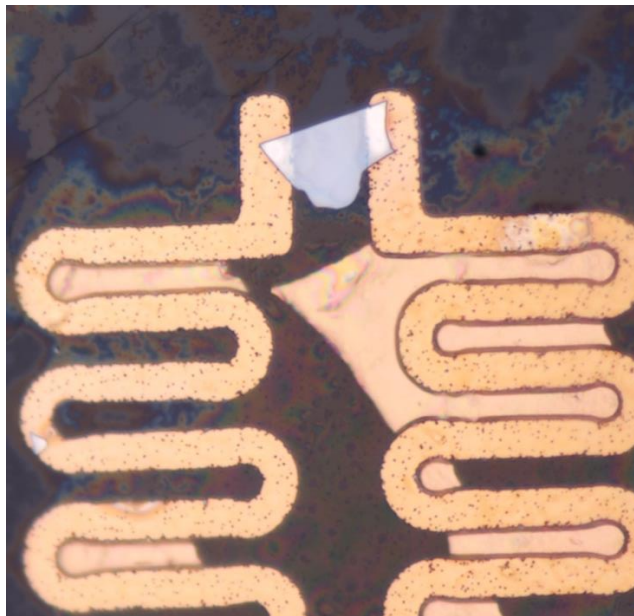


*Figure 5.1 2D material on flexible substrate.*

PDMS is a widely utilized polymer in the fabrication and prototyping of microfluidic chips due to its advantageous properties. It belongs to the siloxane family, which is a mineral-organic polymer comprising carbon, silicon, and oxygen. PDMS offers exceptional flexibility, transparency, and biocompatibility, making it an ideal candidate for creating flexible substrates for micro devices. Its unique properties enable the formation of conformal contact with ultra-thin two-dimensional materials, facilitating their integration into flexible structures. The flexibility of the PDMS substrate allows it to conform to various shapes and surfaces[98], ensuring compatibility with the mechanical properties of 2D flakes. This compatibility is crucial in preserving the structural integrity and functionality of the integrated micro device, even when subjected to bending, stretching, or other mechanical deformations. Additionally, PDMS provides an insulating and protective layer that shields the delicate two-dimensional material from environmental factors,

ensuring its longevity and reliability.

## 5.2 How to Increase Adhesion

The integration of vdW devices with polymer substrates, such as PDMS, presents a significant challenge due to the inherent weak adhesion resulting from the dangling bond-free surfaces of vdW devices[10]. While polymer supporting substrates offer advantages in terms of mechanical strength and ease of handling, the lack of strong chemical bonds between the vdW device and the polymer substrate hinders their adhesion.

To overcome this issue, researchers have explored various strategies to enhance the bonding between vdW devices and polymer substrates. Initially, a common method involved using clips to clamp the sample on both sides[99]. However, this approach proved to be unstable as it failed to ensure simultaneous stretching of the flexible substrate and the upper flake. The absence of real adhesion between these components led to undesired sliding between the layers. Another approach employed by some research groups involved using a spin coater to encapsulate the surface of the sample[100], aiming to firmly fix the sample flake onto the flexible substrate. While this method improves adhesion, it imposes limitations on the fabrication of flexible micro devices and restricts diverse development directions.

In contrast, we propose an alternative approach based on surface modifications, where chemical treatments are utilized to modify the surface properties of either the polymer substrate or the vdW device. These modifications involve introducing functional groups or adhesion-promoting molecules, facilitating stronger intermolecular interactions and enhancing adhesion. This innovative technique addresses the challenge of weak adhesion, providing a promising solution for the integration of vdW devices with polymer substrates.

## 5.3 Au-MPTMS Method

### 5.3.1 Principle

Van der Waals (vdW) solids have been extensively studied, and their cleavage surfaces are naturally passivated by chalcogen anions. These anions have a strong affinity for forming robust coordinate chemical bonds with various metals, including gold, silver, and other counterparts. Taking inspiration from this intriguing phenomenon, we propose an innovative approach for integrating vdW solids with polymers, represented in Fig. 36. Our design incorporates a multi-step process. Firstly, the surfaces of vdW solids are adorned with gold atoms, which subsequently undergo covalent bonding with (3-mercaptopropyl) trimethoxy silane (MPTMS) molecules using gold-thiolate chemistry[101]. The MPTMS molecules possess trimethoxy silane (-Si-OCH3) groups at the opposite end, allowing them to react with hydroxyl (-OH) functionalities present on the polymer substrate during the cross-linking process. As a result, a secure and reliable anchoring of the gold-activated vdW solids within the polymer matrix is achieved.
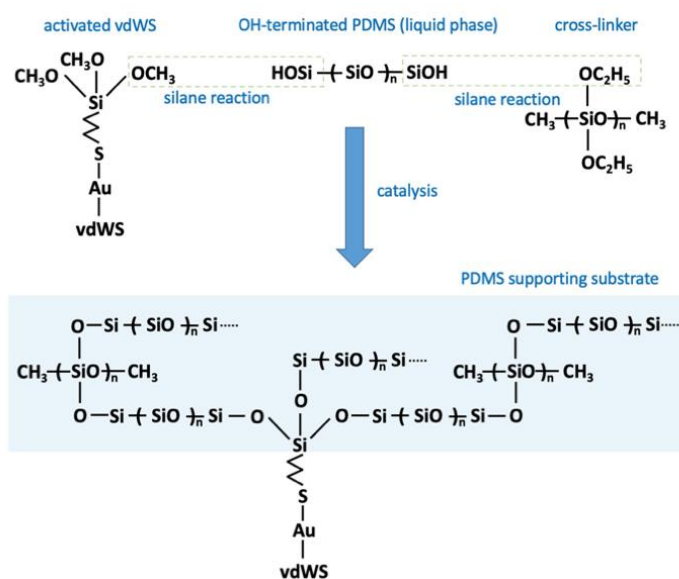


*Figure 5.2 Au-MPTMS method reaction principle.*
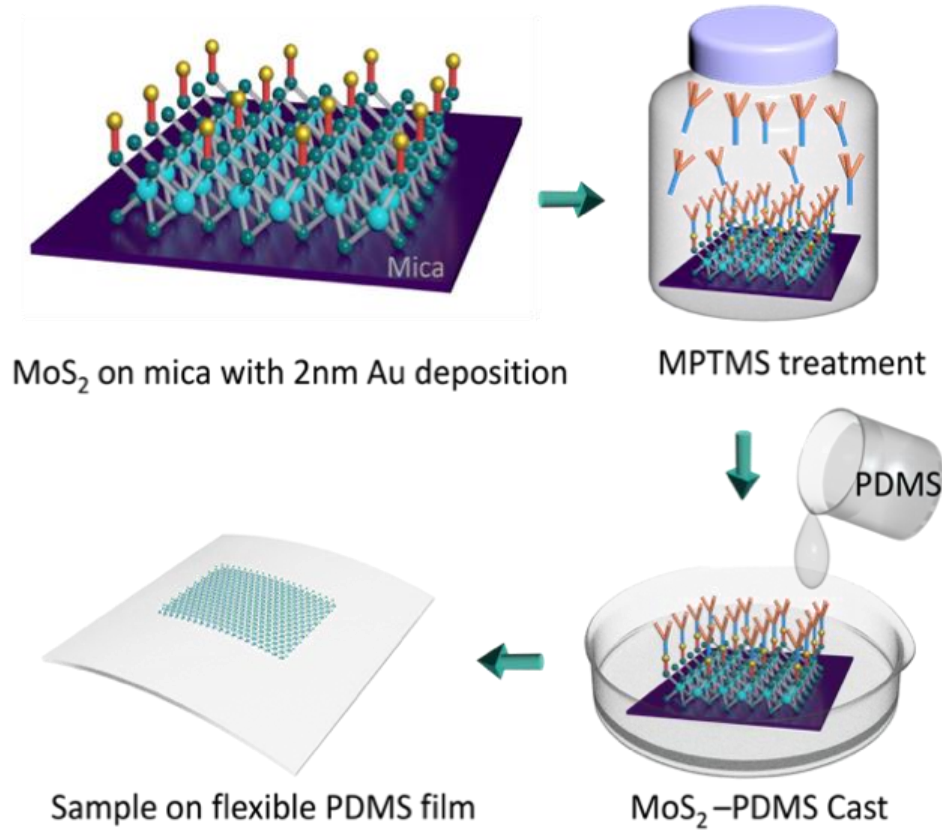
*Figure 5.3 Au-MPTMS method treatment workflow.*

### 5.3.2  *Workflow*

To carry out the proposed design experimentally, we have developed a well-defined process workflow, as depicted in Fig. 37. The versatility of this approach is demonstrated using MoS2 as a representative van der Waals solid (vdWS) and PDMS as the polymer substrate for testing purposes. Initially, mica or poly-(bisphenol A carbonate) (PBAC) substrates are utilized to support the $MoS_2$ samples. Mechanical exfoliation is employed to obtain multi-layer $MoS_2$, while monolayer $MoS_2$ is synthesized through chemical vapor deposition (CVD). Next, a thin layer of gold, with a thickness of 1-2 nm, is thermally deposited on the MoS2 samples. This deposition technique results in discrete gold nanoparticles bonded to the 2D surface, minimally

altering the electronic properties. The scanning transmission electron microscopy (STEM) image

in Fig. 38 clearly reveals the distribution of deposited Au nanoparticles on the sample's surface.
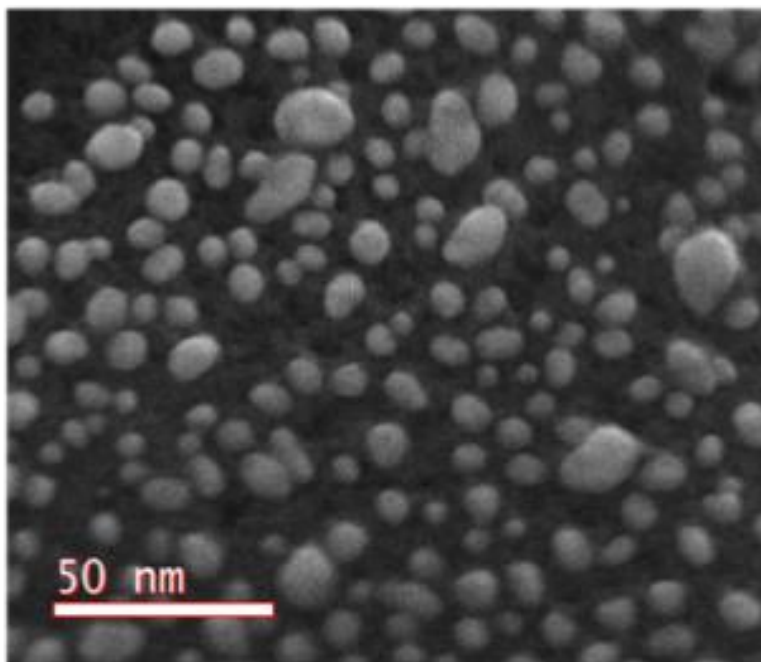


*Figure 5.4 Scanning transmission electron microscopy image of the deposited Au nanoparticles.*

Following the deposition process, the gold-decorated $MoS_2$ samples are enclosed in a

container filled with MPTMS vapor for 3 hours to allow for the formation of a fully covered self-

assembled molecular monolayer. Subsequently, we cast the functionalized $MoS_2$ samples using a

PDMS precursor mixture. The mixture consists of hydroxyl-terminated PDMS (consisting of

uncross-linked molecular chains in the liquid phase), ethylsilicate as a cross-linker, and a catalyst

to expedite the curing process. The presence of hydroxyl groups in the precursor is essential for

successful lamination between $MoS_2$ and PDMS, as they react with MPTMS and establish

anchor points, as depicted in Fig. 36. It is worth noting that commonly used A-B two-part PDMS

kits may not be suitable for this workflow due to the absence of hydroxyl groups.

Moreover, directly laminating the MPTMS-functionalized vdWS layers onto pre-cured PDMS substrates proves challenging, even with the application of oxygen plasma treatment to create hydroxyl functional groups. This is primarily due to the inability of pre-cured PDMS to provide an atomically flat geometry that precisely matches the vdWS surfaces, as illustrated in Fig. 39. The roughness or variations in distances, even at the nanometer scale, are still significant compared to the Angstrom-scale MPTMS molecules, resulting in inadequate anchor points for robust lamination. In contrast, our functionalizing-and-casting procedure overcomes these challenges and enables the fabrication of high-quality vdWS-polymer composite structures for flexible device applications. Following the preparation process, the as-prepared PDMS requires approximately 24 hours to cure at room temperature before subsequent mechanical and electrical tests can be conducted.
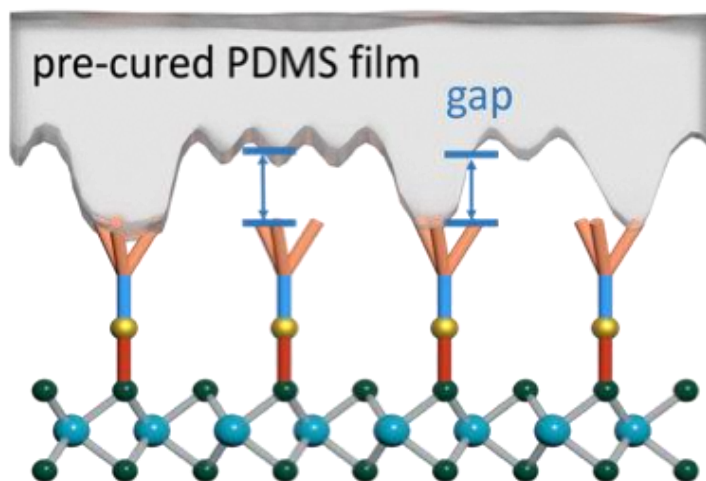


*Figure 5.5 Demonstration of poorer contacts if directly laminate the MPTMS-functionalized vdW-S to a pre-cured PDMS substrate.*

## 5.4    Raman Characterization

To assess the quality of lamination, a tensile test was performed, and the deformation of

MoS$_2$ was monitored using Raman spectroscopy. For the tensile test, a custom-built computer-controlled fixture, as shown in Fig. 40 was employed to stretch the PDMS substrate. The fixture securely clamped the PDMS substrates on both ends, and precise control over the strain was achieved using a step motor with an accuracy of 0.025%. In order to analyze the deformation of MoS$_2$, in-situ Raman spectra were collected during the stretching process.
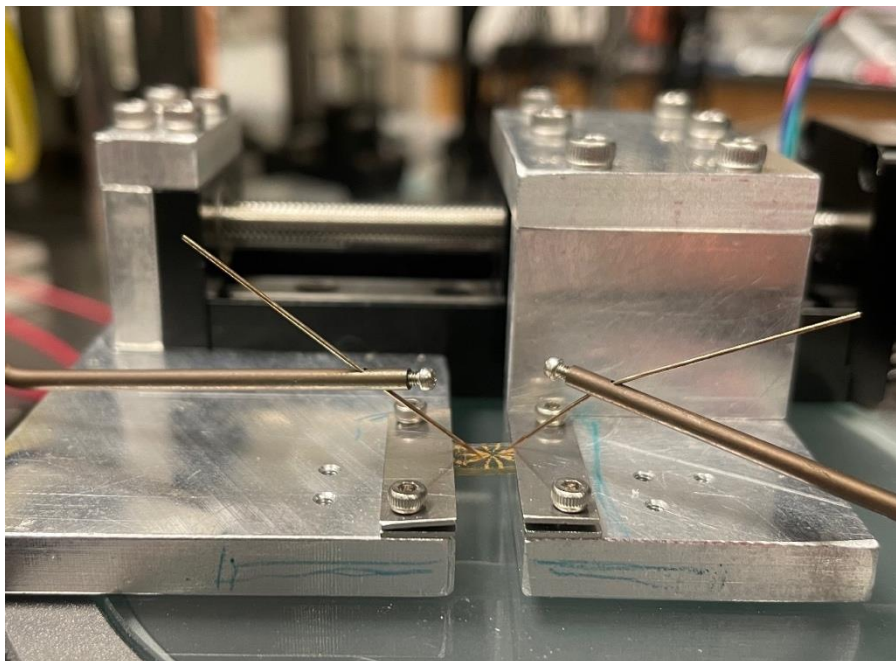


*Figure 5.6 Custom-built computer-controlled stretching stage.*

The characterization focused on MoS$_2$-PDMS samples without any interfacial functionalization, as the PDMS substrate was subjected to stretching, the Raman spectrum displayed minimal changes in peak positions, as illustrated in Fig. 41a and b. This observation indicated a lack of strong interaction between the substrate deformation and the MoS$_2$ flakes, highlighting the presence of weak adhesion at the interface. Furthermore, atomic force microscopy (AFM) analysis clearly demonstrated the formation of wrinkles on the vdWS layers following the stretching test, as depicted in Fig. 41c. On the other hand, samples that underwent interfacial

functionalization, regardless of the thickness of the MoS$_2$ flakes, showed significant Raman peak

shifting when strains were applied to the PDMS substrates, as illustrated in Fig. 41d to 41g. This

observation was in accordance with our anticipated outcomes.
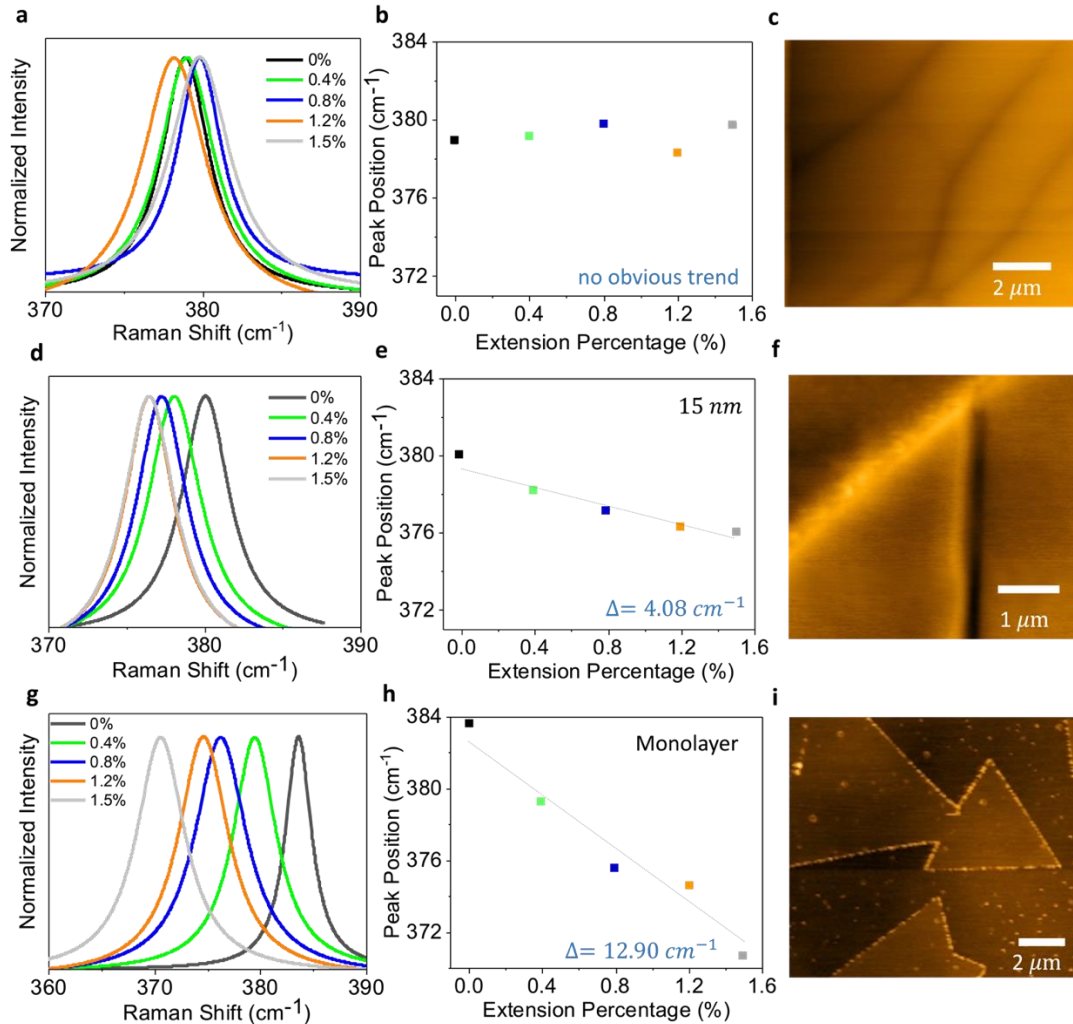


*Figure 5.7 Lamination quality characterization for different MoS2-PDMS samples. (a) Raman spectrum of control sample without interfacial functionalization under different tensile strains. (b) The corresponding peak positions obtained from (a) under different tensile strains. Under the action of continuously increasing tensile percentage, the irregular Raman shifting appears because of the existence of interlayer slipper caused by weak bonding. (c) AFM mapping of the sample without Au deposition and MPTMS treatment after stretching. (d) Raman spectrum of 15 nm examined MoS$_2$ sample under different tensile strains. A subtle redshift phenomenon can be observed. (e) The corresponding peak positions obtained from (d) under different tensile strains. The Raman peak shifting magnitude is 4.08 cm$^{-1}$ from 0% to 1.5% strain. The linear fitting curve is shown as the black line. (f) AFM mapping of the 15 nm examined MoS$_2$ examined sample in (d) after stretching. (g) Raman spectrum of monolayer examined CVD-MoS$_2$*

*sample under different tensile strains. A obvious redshift phenomenon can be observed. (h) The corresponding peak positions obtained from (g) under different tensile strains. The Raman peak shifting magnitude is 12.90 cm$^{-1}$ from 0% to 1.5% strain. The linear fitting curve is shown as the black line. (i) AFM mapping of the examined CVD-MoS$_2$ sample in (g) after stretching.*

# 6    CHAPTER 6 FLEXIBLE MICRO DEVICE FABRICATION

## 6.1    Flexible Device Application and Background

Flexible electronics has emerged as a highly promising and revolutionary technology for advanced manufacturing and product development, garnering significant interest from academia, industry, and government sectors in the past decade. The appeal of flexible electronics lies in its distinctive advantages in terms of fabrication and functionality. The ability to achieve low-cost, large-area processing and facile fabrication configurability provides a compelling cost-effectiveness and flexibility for high-volume production. Furthermore, the lightweight nature, shape adaptability, and mechanical softness of flexible electronics enable functionalities that are unattainable with conventional rigid electronics based on complementary metal-oxide-semiconductor (CMOS) technology.

The inception of electronics incorporating mechanically flexible active materials can be traced back to the 1960s[102], when efforts were initiated to reduce the thickness and weight of monocrystalline silicon solar cells for aerospace applications. Despite the successful exploration of large-area, cost-effective processing of organic printed electronics in the 1990s, the mechanical flexibility of these thin-film electronic systems did not receive substantial attention. However, over the past 15 years, there has been a remarkable acceleration in the field of flexible electronics, driven by the escalating demand for shape adaptability and interface softness in diverse domains such as advanced healthcare, human-machine interfaces, and the Internet of Things. This period has witnessed the rapid establishment of a diverse repertoire of flexible devices, encompassing integrated circuit components (inverters, ring oscillators, amplifiers, data/power transmission circuits, memories, etc.) and environmental interaction units (energy harvesting and storage devices, sensors, displays, actuators, etc.). Moreover, the concept of

mechanical flexibility has transcended conventional bendability, with the advent of foldable, twistable, wrinkle-resistant, and stretchable devices becoming pervasive.

In addition, substantial research endeavors in the realm of soft functional materials have propelled the field of bioelectronics, enabling seamless integration of electronic components with delicate biological tissues. This paradigm shift has unlocked new frontiers for developing imperceptible electronic interfaces with biological systems, heralding transformative opportunities in various applications.

## 6.2    Flexible Device Fabrication Difficulties

The industrial adoption of flexible electronics is contingent upon two key factors: device performance, and manufacturing capability. Crucially, the viability of flexible electronic devices hinges upon their ability to exhibit robust mechanical durability (including wear resistance and fatigue resistance), electrical durability (such as extended service life and on-off cycling capabilities), and environmental durability (such as resilience to humidity and extreme temperatures) to meet the rigorous demands of real-world applications.

Furthermore, the development of consumer-oriented system-level integrated functional devices remains a significant challenge[103]. While there have been notable advancements in the integration of flexible systems in recent years, the majority of reported devices still rely on additional components to achieve optimal functionality. This underscores the need for concerted efforts to realize fully integrated flexible systems that encompass all the requisite functionalities without external dependencies. Under the mainstream trend of continuous miniaturization and flexibility of semiconductor devices, 2D materials represented by transition metal chalcogenides (TMDC) such as molybdenum disulfide ($MoS_2$) show unique advantages as for the key material for the next generation of semiconductor devices. 2D materials have ultra-thin thickness (single

atomic layer or few atomic layers), excellent electrical, optical, mechanical properties, and multi-degree-of-freedom controllability, making them lighter, thinner, faster, and more sensitive. However, at this stage, there are still two key scientific problems in the research of device application: 1. Material preparation—how to obtain high-quality and large-scale wafers; 2. Device technology—How to achieve high-density, high-performance, large-area uniform device processing. This is a common problem that new semiconductor materials have to go through from the laboratory to the market. If the key scientific obstacles to its high-quality large-scale preparation and integrated device performance regulation can be solved, it will definitely promote the application and development of 2D materials, giving flexible electronics industry injects new impetus for development. Therefore, suitable materials and optimized micro fabrication processes are two crucial conditions for the development of flexible devices, which is the significance of the research involved in this thesis.

## 6.3 Au-MPTMS Assistant Fabrication Method

### 6.3.1 Principle and Workflow

The successful application of interfacial chemical bonding demonstrated in the previous experiments goes beyond the lamination of vdW-S and polymers. It offers a solution to a significant challenge encountered in the fabrication of flexible devices. The soft nature of polymer substrates makes them prone to deformation during conventional processes designed for rigid semiconductors, such as spin coating and lithography. This deformation can compromise the precision and scalability of the manufacturing process.

In contrast, the principle of interfacial chemical bonding allows for the relocation and attachment of fully fabricated vdW-S-based electronics or rigid substrates onto polymers, enabling

the construction of flexible devices. This approach brings about a substantial improvement in the precision and scalability of the fabrication process. Additionally, the resulting devices exhibit exceptional quality, providing a unique opportunity to gain valuable insights into the evolution of electronic properties in vdW-S materials under mechanical deformation.
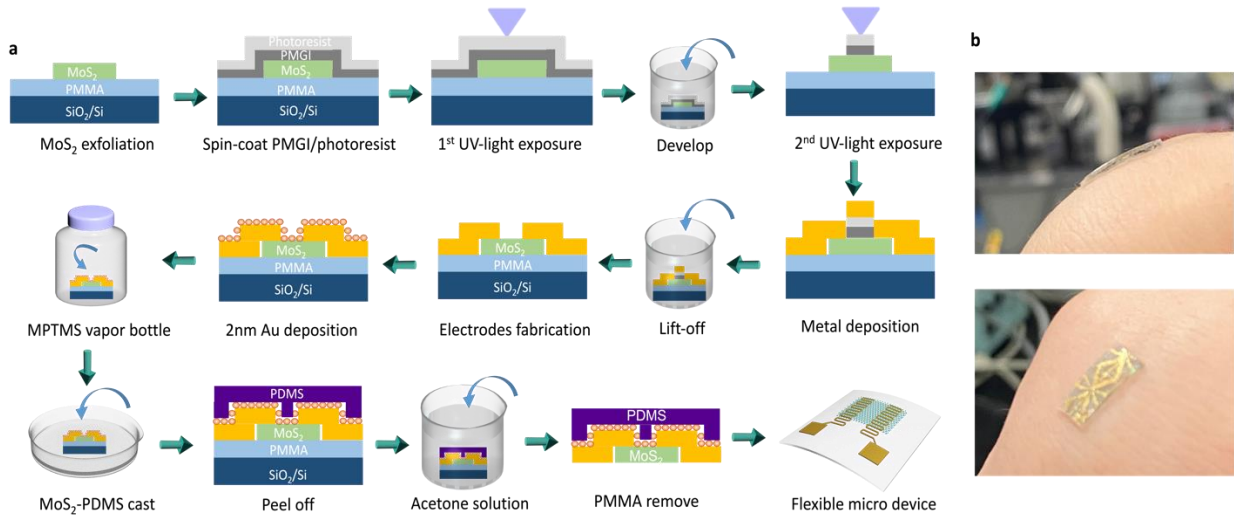


*Figure 6.1 Interfacial functionalization-based flexible device fabrication technology and device-skin fit adaptability display. (a) Workflow of device fabrication, relocation, and lamination process. (b) Side and front views of the adaptability of flexible device obtained from interfacial functionalization strategy to human skin while bending force applied.*

The workflow for device fabrication, relocation, and lamination process is depicted in Fig. 42. Initially, mechanically exfoliated vdWS are transferred onto flat rigid substrates coated with poly(methylmethacrylate) (PMMA), such as Si/SiO$_2$. The PMMA coating serves as a sacrificial layer for the subsequent separation of the flexible devices. To generate electrode patterns, a regular photolithography process is employed using S1805 photoresist and a polydimethylglutarimide (PMGI) undercut layer. The developed photoresist pattern is exposed to UV light for a second time before metal deposition. Following the metal deposition, an alkaline-based developer is used to remove the double-exposed S1805 photoresist for metal deposition lift-off, avoiding the use of acetone and other commonly used organic solvents to preserve the

PMMA coating. Subsequently, a thin layer of gold, approximately 1-2 nm in thickness, is deposited on the structure, followed by MPTMS functionalization and PDMS casting. After the PDMS cures, acetone is utilized to dissolve the PMMA coating and release the flexible devices. The devices produced through this procedure exhibit exceptional mechanical flexibility and conform well to human skin even under various motion conditions, as illustrated in Fig. 42b. Therefore, our method fully utilizes the inherent flexibility and stretchability of vdW-S devices, enabling their application in medical treatment motion control, biosensors, and other critical fields.

### 6.3.2   *Performance*

Upon successful construction of the flexible device, a comprehensive set of optoelectronic characterizations was conducted to evaluate its performance, with particular focus on the effects of interfacial lamination and mechanical deformation. Photoresponse spectra were employed as a direct measure of the energy band structure of the vdW-S material, revealing crucial insights into the impacts of lamination and deformation. As depicted in Fig. 43a, the photocurrent of the MoS2 device demonstrated a pronounced wavelength dependence. Notably, it exhibited a strong response to blue light in the visible light region. Additionally, a response peak at 650 nm was observed, corresponding to intra-band excitation. These findings are consistent with previously reported MoS2 photoresponse spectra, validating the semiconductor characteristics of the laminated MoS2 despite the thin gold deposition. Moreover, these results confirm that the 1~2 nm gold deposition effectively provides discrete isolated anchor points, rather than forming a continuous conductive film, facilitating successful MPTMS functionalization.
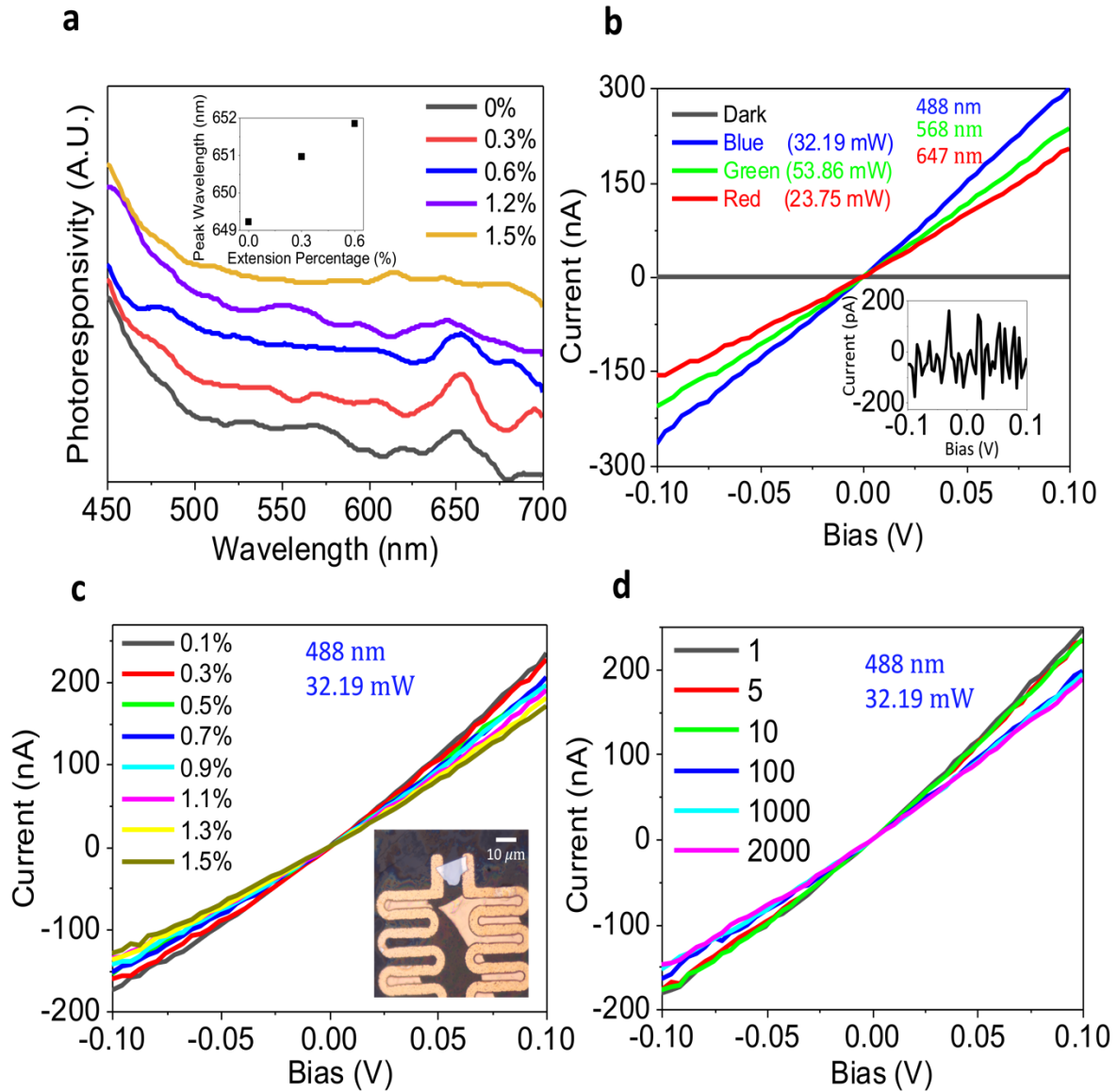
*Figure 6.2 Optoelectronic characterizations of the flexible and stretchable device. (a) Normalized photoresponsivity (P.R.) spectra of the relocated flexible device with a bias voltage of 0.1 V. (inset) Slightly red-shift trend of the 650nm peak until the tensile reaches 0.6%. (b) Photocurrent curves of the relocated flexible device excited by red (647 nm), green (568 nm), and blue (488 nm) laser light sources with a bias voltage of ±0.1 V and without tensile strains. (inset) Dark current curve. (c) Photocurrent curves of the relocated flexible device under different tensile strains with a bias voltage of 0.1 V. The photocurrent value fluctuates slightly during the stretching process. The excitation laser wavelength is 488nm. (inset) Optical image of the relocated flexible and stretchable device. (d) Photocurrent curves of the relocated flexible device under multiple cyclic stretching tests while the strain up to 1.5%. The photocurrent values attenuated slightly during the multiple stretching-relaxing processes. The excitation laser wavelength is 488nm.*

As the strain is increased, the photoresponse spectra demonstrate that MoS2 maintains its semiconductor properties even up to a strain of 1.5%. Notably, the response peak at 650 nm persists until a strain of 0.6% and then disappears. Upon closer examination, a slight red shift is observed as the strain increases (inset of Fig. 43a a). These findings align precisely with an earlier theoretical simulation, indicating the efficient coupling of PDMS strain to the MoS2 devices through covalent bonding at their interfaces.

In addition to the spectral study, photoconductivity (I-V) measurements were conducted and depicted in Fig. 43b. Initially, the $MoS_2$ device was excited successively with red (647 nm), green (568 nm), and blue (488 nm) laser sources without applying any tensile strain. The device exhibited distinct responses to all three excitations, with photoresponsivity values of 4.18 (A/W), 1.63 (A/W), and 4.55 (A/W) for red, green, and blue lights, respectively, within a bias voltage range of ± 0.1 V. The linearity of the I-V curves confirms a good ohmic-like contact between MoS2 and the gold electrodes, as suggested by previous investigations. Furthermore, the dark current of the device (inset of Figure Fig. 43b) was found to be extremely low, approaching the noise level of the experimental setup. This low dark current further verifies that the 1~2 nm gold deposition and MPTMS functionalization do not create any conductive channels that would hinder device performance.

Fig. 43c presents the photocurrent response as a function of tensile strain, with the optical microscope image of the device shown in the inset. A 488 nm excitation was utilized for this investigation. It was observed that the I-V curves gradually decrease as the strain increases but remain within the same order of magnitude with less than a 20% variation. To better understand this change, a mechanical cycling test was performed, measuring the photocurrent levels after 1, 5, 10, 100, 1000, and 2000 cycles of tensile strain up to 1.5%, as depicted in Fig. 43d.

Remarkably, no significant degradation in photocurrent was observed during these mechanical cycling tests, and the photocurrent returned to its original level after the strain was removed. These experiments confirm the outstanding mechanical robustness and endurance of the device architecture achieved through our fabrication strategy. It can be concluded that the decreased photocurrent level with increasing strain is not due to loss of contacts, material peeling, or other structural issues. Instead, it could be attributed to variations in the band structure, resulting in lower photoresponsivity.

# 7 CONCLUSION

This thesis has made significant contributions to the fabrication of miniature flexible devices utilizing van der Waals materials. Through a comprehensive range of experiments, the characteristics of van der Waals materials were thoroughly investigated, the manufacturing process of lithography technology was optimized, and the photoelectric performance of micro devices was meticulously characterized. As a result, the development of micro flexible device manufacturing has been advanced, and its applications have been expanded in various fields such as biological detection, medical treatment, and environmental monitoring. The introduction of a miniature van der Waals materials empowered vertical color sensor. with its unique vertical structure, occupies three times less volume space compared to traditional planar color sensors. Moreover, it incorporates multiple optical aberration correction functions, enabling improved color recognition. Moreover, a novel chemical treatment method involving gold nanoparticles and (3-mercaptopropyl)trimethoxysilane (MPTMS) was proposed, enabling the relocation of flexible micro devices, and significantly enhances the adhesion between the 2D material layer and the flexible substrate. Thereby greatly increasing the stretchability and durability of the flexible devices. These advancements in device fabrication processes and material flexibility provide promising prospects for the development of smart wearable devices, biomedical detection systems, and other related fields.

# REFERENCES

1. Margenau, H., *Van der Waals forces.* Reviews of Modern Physics, 1939. **11**(1): p. 1.
2. Yabuki, N., et al., *Supercurrent in van der Waals Josephson junction.* Nature communications, 2016. **7**(1): p. 10616.
3. Castellanos-Gomez, A., et al., *Van der Waals heterostructures.* Nature Reviews Methods Primers, 2022. **2**(1): p. 58.
4. Geim, A.K. and K.S. Novoselov, *The rise of graphene.* Nature materials, 2007. **6**(3): p. 183-191.
5. Meyer, J.C., et al., *The structure of suspended graphene sheets.* Nature, 2007. **446**(7131): p. 60-63.
6. Yu, W., et al., *Flexible 2D materials beyond graphene: synthesis, properties, and applications.* Small, 2022. **18**(14): p. 2105383.
7. Akinwande, D., N. Petrone, and J. Hone, *Two-dimensional flexible nanoelectronics.* Nature communications, 2014. **5**(1): p. 5678.
8. Senefelder, A., *The invention of lithography*. 1911: Fuchs & Lang Manufacturing Company.
9. Zaouk, R., B.Y. Park, and M.J. Madou, *Introduction to microfabrication techniques.* Microfluidic Techniques: Reviews and Protocols, 2006: p. 5-15.
10. Liu, Y., Y. Huang, and X. Duan, *Van der Waals integration before and beyond two-dimensional materials.* Nature, 2019. **567**(7748): p. 323-333.
11. Liu, Y., et al., *Approaching the Schottky–Mott limit in van der Waals metal–semiconductor junctions.* Nature, 2018. **557**(7707): p. 696-700.
12. Jariwala, D., T.J. Marks, and M.C. Hersam, *Mixed-dimensional van der Waals heterostructures.* Nature materials, 2017. **16**(2): p. 170-181.
13. Okmi, A., et al., *How surface tension matters in polymer-free graphene transfer.* Oxford Open Materials Science, 2021. **1**(1): p. itab007.
14. Li, N., et al., *van der Waals Semiconductor Empowered Vertical Color Sensor.* ACS nano, 2022. **16**(6): p. 8619-8629.
15. Lei, S., et al., *Evolution of the electronic band structure and efficient photo-detection in atomic layers of InSe.* ACS nano, 2014. **8**(2): p. 1263-1272.
16. Lei, S., et al., *Ternary CuIn7Se11: Towards Ultra‐Thin Layered Photodetectors and Photovoltaic Devices.* Advanced Materials, 2014. **26**(45): p. 7666-7672.
17. Huang, Z., et al., *A general theory for the bending of multilayer van der Waals materials.* Journal of the Mechanics and Physics of Solids, 2023. **171**: p. 105144.
18. Cheng, R., et al., *High-performance, multifunctional devices based on asymmetric van der Waals heterostructures.* Nature Electronics, 2018. **1**(6): p. 356-361.
19. Schaller, R.R., *Moore's law: past, present and future.* IEEE spectrum, 1997. **34**(6): p. 52-59.
20. Eder, J.M., *XIX. Joseph Nicephore Niepce*, in *History of Photography*. 1945, Columbia University Press. p. 193-207.
21. Bakshi, V., *EUV lithography.* 2009.
22. Henderson, R., *Underinvestment and incompetence as responses to radical innovation: Evidence from the photolithographic alignment equipment industry.* The RAND Journal of Economics, 1993: p. 248-270.

23. Wyss, H. *Pioneering work on low power low voltage CMOS technology and design performed in Switzerland, 1966–1980.* in *2019 6th IEEE History of Electrotechnology Conference (HISTELCON).* 2019. IEEE.

24. Maldonado, J.R. and M. Peckerar, *X-ray lithography: Some history, current status and future prospects.* Microelectronic Engineering, 2016. **161**: p. 87-93.

25. Kinoshita, H., *History of extreme ultraviolet lithography.* Journal of Vacuum Science & Technology B: Microelectronics and Nanometer Structures Processing, Measurement, and Phenomena, 2005. **23**(6): p. 2584-2588.

26. Van de Kerkhof, M., J. Benschop, and V. Banine, *Lithography for now and the future.* Solid-State Electron, 2019. **155**: p. 20-26.

27. Stephens, F.G., *Artists at Home Photographed by JP Mayall, and Reproduced in Facsimile by Photo-engraving, on Copper Plates.* 1884: Appleton.

28. Qin, D., et al., *Photolithography with transparent reflective photomasks.* Journal of Vacuum Science & Technology B: Microelectronics and Nanometer Structures Processing, Measurement, and Phenomena, 1998. **16**(1): p. 98-103.

29. Bellah, M.M., S.M. Christensen, and S.M. Iqbal, *Nanostructures for medical diagnostics.* Journal of Nanomaterials, 2012. **2012**: p. 1-21.

30. Madou, M.J., *Manufacturing techniques for microfabrication and nanotechnology.* 2011: CRC press.

31. Dalawai, S.P., et al., *Recent advances in durability of superhydrophobic self-cleaning technology: a critical review.* Progress in Organic Coatings, 2020. **138**: p. 105381.

32. Lim, E., et al. *Design of anti-theft/cable cut real time alert system for copper cable using microcontroller and GSM technology.* in *AIP Conference Proceedings.* 2017. AIP Publishing LLC.

33. Zhong, J., et al., *Self-powered human-interactive transparent nanopaper systems.* ACS nano, 2015. **9**(7): p. 7399-7406.

34. Park, T.H. and M.L. Shuler, *Integration of cell culture and microfabrication technology.* Biotechnology progress, 2003. **19**(2): p. 243-253.

35. Gu, L., et al., *A biomimetic eye with a hemispherical perovskite nanowire array retina.* Nature, 2020. **581**(7808): p. 278-282.

36. Zhou, F., et al., *Optoelectronic resistive random access memory for neuromorphic vision sensors.* Nature nanotechnology, 2019. **14**(8): p. 776-782.

37. Pei, Y., et al., *Artificial visual perception nervous system based on low-dimensional material photoelectric memristors.* ACS nano, 2021. **15**(11): p. 17319-17326.

38. Cianchetti, M. and C. Laschi, *Pleasant to the touch: by emulating nature, scientists hope to find innovative new uses for soft robotics in health-care technology.* IEEE pulse, 2016. **7**(3): p. 34-37.

39. Martinez-Cisneros, C.S., et al., *Ultracompact three-dimensional tubular conductivity microsensors for ionic and biosensing applications.* Nano letters, 2014. **14**(4): p. 2219-2224.

40. Cianchetti, M., et al., *Biomedical applications of soft robotics.* Nature Reviews Materials, 2018. **3**(6): p. 143-153.

41. Wang, Y., et al., *Memristor-based biomimetic compound eye for real-time collision detection.* Nature Communications, 2021. **12**(1): p. 5979.

42. Xia, Q. and J.J. Yang, *Memristive crossbar arrays for brain-inspired computing.* Nature materials, 2019. **18**(4): p. 309-323.

43. Kumar, M., et al., *PulseCam: a camera-based, motion-robust and highly sensitive blood perfusion imaging modality.* Scientific reports, 2020. **10**(1): p. 1-17.

44. Lew, T.T.S., et al., *Real-time detection of wound-induced H2O2 signalling waves in plants with optical nanosensors.* Nature plants, 2020. **6**(4): p. 404-415.

45. Wang, Y., et al., *Cephalopod-inspired chromotropic ionic skin with rapid visual sensing capabilities to multiple stimuli.* ACS nano, 2021. **15**(2): p. 3509-3521.

46. Fent, L. and A. Meldrum, *A foveon sensor/green-pass filter technique for direct exposure of traditional false color images.* Journal of Imaging, 2016. **2**(2): p. 14.

47. Lukas, J., J. Fridrich, and M. Goljan, *Digital camera identification from sensor pattern noise.* IEEE Transactions on Information Forensics and Security, 2006. **1**(2): p. 205-214.

48. Zhang, K., et al., *Self-induced uniaxial strain in MoS2 monolayers with local van der Waals-stacked interlayer interactions.* ACS nano, 2015. **9**(3): p. 2704-2710.

49. Son, S., et al., *Strongly adhesive dry transfer technique for van der Waals heterostructure.* 2D Materials, 2020. **7**(4): p. 041005.

50. Liu, Y., et al., *Van der Waals heterostructures and devices.* Nature Reviews Materials, 2016. **1**(9): p. 1-17.

51. Ahrenkiel, R.K., *The Race to Electronic Photography.* Optics and Photonics News, 2023. **34**(5): p. 46-53.

52. Zhang, W., et al., *Van der Waals stacked 2D layered materials for optoelectronics.* 2D Materials, 2016. **3**(2): p. 022001.

53. Yang, S.-J., et al., *All-dry transfer of graphene film by van der Waals interactions.* Nano letters, 2019. **19**(6): p. 3590-3596.

54. Sakai, O., et al., *In-vacuum active colour sensor and wireless communication across a vacuum-air interface.* Scientific Reports, 2021. **11**(1): p. 1364.

55. Lee, J.Y. and S.I. Yoo. *An elliptical boundary model for skin color detection*. in *Proc. of the 2002 International Conference on Imaging Science, Systems, and Technology*. 2002. Citeseer.

56. Pepe, M., L. Fregonese, and M. Scaioni, *Planning airborne photogrammetry and remote-sensing missions with modern platforms and sensors.* European Journal of Remote Sensing, 2018. **51**(1): p. 412-436.

57. Wickramaratne, D., F. Zahid, and R.K. Lake, *Electronic and thermoelectric properties of van der Waals materials with ring-shaped valence bands.* Journal of Applied Physics, 2015. **118**(7): p. 075101.

58. Mashiko, H., et al., *Petahertz optical drive with wide-bandgap semiconductor.* Nature physics, 2016. **12**(8): p. 741-745.

59. McRaven, C., *The Blacksmith's Craft: A Primer of Tools & Methods*. 2005: Storey Publishing, LLC.

60. Bockelée-Morvan, D., et al., *VIRTIS-H observations of the dust coma of comet 67P/Churyumov-Gerasimenko: spectral properties and color temperature variability with phase and elevation.* Astronomy & Astrophysics, 2019. **630**: p. A22.

61. Wyszecki, G. and W. Stiles, *Color Science. vol. 8 Wiley.* New York, 1982.

62. Rowlands, D.A., *Color conversion matrices in digital cameras: a tutorial.* Optical Engineering, 2020. **59**(11): p. 110801-110801.

63. Rahman, S., et al., *An adaptive gamma correction for image enhancement.* EURASIP Journal on Image and Video Processing, 2016. **2016**(1): p. 1-13.

64.     Nguyen, K.T., et al., *A Magnetically Guided Self‑Rolled Microrobot for Targeted Drug Delivery, Real‑Time X‑Ray Imaging, and Microrobot Retrieval.* Advanced Healthcare Materials, 2021. **10**(6): p. 2001681.

65.     Palagi, S. and P. Fischer, *Bioinspired microrobots.* Nature Reviews Materials, 2018. **3**(6): p. 113-124.

66.     Nocentini, S., et al., *Optically driven soft micro robotics.* Advanced Optical Materials, 2018. **6**(14): p. 1800207.

67.     Pawashe, C., S. Floyd, and M. Sitti, *Modeling and experimental characterization of an untethered magnetic micro-robot.* The International Journal of Robotics Research, 2009. **28**(8): p. 1077-1094.

68.     Yang, Z., et al., *Wafer-scale synthesis of high-quality semiconducting two-dimensional layered InSe with broadband photoresponse.* ACS nano, 2017. **11**(4): p. 4225-4236.

69.     Liu, K., et al., *A wafer-scale van der Waals dielectric made from an inorganic molecular crystal film.* Nature Electronics, 2021. **4**(12): p. 906-913.

70.     Jin, G., et al., *Atomically thin three-dimensional membranes of van der Waals semiconductors by wafer‑scale growth.* Science Advances, 2019. **5**(7): p. eaaw3180.

71.     Hu, C., et al., *Wafer-scale sulfur vacancy-rich monolayer MoS2 for massive hydrogen production.* The Journal of Physical Chemistry Letters, 2019. **10**(16): p. 4763-4768.

72.     French, A. *Issac Newton: A passion to learn and understand*. in *AIP Conference Proceedings*. 1988. American Institute of Physics.

73.     Masters, B.R., *A brief history of spectral analysis and astrospectroscopy.* Optics and Photonics News, 2009. **20**(11): p. 34-39.

74.     Welz, B., et al., *Continuum source atomic absorption spectrometry: past, present and future aspects-a critical review.* Journal of the Brazilian Chemical Society, 2014. **25**: p. 799-821.

75.     Beutler, H., *The theory of the concave grating.* JOSA, 1945. **35**(5): p. 311-350.

76.     Herold, M., et al., *Spectrometry for urban area remote sensing—Development and analysis of a spectral library from 350 to 2400 nm.* Remote sensing of environment, 2004. **91**(3-4): p. 304-319.

77.     Critchley, A., et al., *The proton transfer reaction mass spectrometer and its use in medical science: applications to drug assays and the monitoring of bacteria.* International Journal of Mass Spectrometry, 2004. **239**(2-3): p. 235-241.

78.     Parsons, P.J. and F. Barbosa Jr, *Atomic spectrometry and trends in clinical laboratory medicine.* Spectrochimica Acta Part B: Atomic Spectroscopy, 2007. **62**(9): p. 992-1003.

79.     Finehout, E.J. and K.H. Lee, *An introduction to mass spectrometry applications in biological research.* Biochemistry and molecular biology Education, 2004. **32**(2): p. 93-100.

80.     Persky, M., *A review of spaceborne infrared Fourier transform spectrometers for remote sensing.* Review of Scientific Instruments, 1995. **66**(10): p. 4763-4797.

81.     Uhov, A., et al. *Use of compact spectrometer for plasma emission qualitative analysis*. in *Journal of Physics: Conference Series*. 2014. IOP Publishing.

82.     St. Louis, R.H., H.H. Hill Jr, and G.A. Eiceman, *Ion mobility spectrometry in analytical chemistry.* Critical Reviews in Analytical Chemistry, 1990. **21**(5): p. 321-355.

83.     Hamilton, S.E., et al., *Use of a miniature mass spectrometer to support pharmaceutical process chemistry.* Organic Process Research & Development, 2014. **18**(1): p. 103-108.

84.     Burgers, A.P., *Towards Quantum Teleportation from a Spontaneous Parametric Down-Conversion Source to a Quantum Dot Spin by Hong-Ou-Mandel Interference*. 2015.

85.     Li, X., et al., *Controlled vapor phase growth of single crystalline, two-dimensional GaSe crystals with high photoresponse.* Scientific reports, 2014. **4**(1): p. 5497.

86.     Zhu, C., et al., *Synthesis and growth of GaSe single crystals.* Journal of Crystal Growth, 2015. **421**: p. 53-57.

87.     Chen, Y., X.L. Gong, and J.G. Gai, *Progress and challenges in transfer of large‐area graphene films.* Advanced science, 2016. **3**(8): p. 1500343.

88.     Suk, J.W., et al., *Transfer of CVD-grown monolayer graphene onto arbitrary substrates.* ACS nano, 2011. **5**(9): p. 6916-6924.

89.     Kim, S.J., et al., *Materials for flexible, stretchable electronics: graphene and 2D materials.* Annual Review of Materials Research, 2015. **45**: p. 63-84.

90.     Du, J., et al., *Strain engineering in 2D material‐based flexible optoelectronics.* Small Methods, 2021. **5**(1): p. 2000919.

91.     Gao, L., *Flexible device applications of 2D semiconductors.* Small, 2017. **13**(35): p. 1603994.

92.     Xue, Q., et al., *Recent progress on flexible and wearable supercapacitors.* Small, 2017. **13**(45): p. 1701827.

93.     Chaudhary, V., et al., *Towards 5th generation ai and iot driven sustainable intelligent sensors based on 2d mxenes and borophene.* ECS Sensors Plus, 2022. **1**(1): p. 013601.

94.     Dong, K., X. Peng, and Z.L. Wang, *Fiber/fabric‐based piezoelectric and triboelectric nanogenerators for flexible/stretchable and wearable electronics and artificial intelligence.* Advanced Materials, 2020. **32**(5): p. 1902549.

95.     Huo, C., et al., *2D materials via liquid exfoliation: a review on fabrication and applications.* Science bulletin, 2015. **60**(23): p. 1994-2008.

96.     Yang, W., et al., *3D printing of freestanding MXene architectures for current‐collector‐free supercapacitors.* Advanced materials, 2019. **31**(37): p. 1902725.

97.     Kim, C., et al., *Damage-free transfer mechanics of 2-dimensional materials: competition between adhesion instability and tensile strain.* NPG Asia Materials, 2021. **13**(1): p. 44.

98.     Yang, H., et al., *Graphene: diversified flexible 2D material for wearable vital signs monitoring.* Advanced Materials Technologies, 2019. **4**(2): p. 1800574.

99.     Conley, H.J., et al., *Bandgap engineering of strained monolayer and bilayer MoS2.* Nano letters, 2013. **13**(8): p. 3626-3630.

100.    Li, Z., et al., *Efficient strain modulation of 2D materials via polymer encapsulation.* Nature communications, 2020. **11**(1): p. 1151.

101.    Häkkinen, H., *The gold–sulfur interface at the nanoscale.* Nature chemistry, 2012. **4**(6): p. 443-455.

102.    Lembke, D., S. Bertolazzi, and A. Kis, *Single-layer MoS2 electronics.* Accounts of chemical research, 2015. **48**(1): p. 100-110.

103.    Moonen, P.F., I. Yakimets, and J. Huskens, *Fabrication of transistors on flexible substrates: from mass‐printing to high‐resolution alternative lithography strategies.* Advanced materials, 2012. **24**(41): p. 5526-5541.

104.    Sang, X., et al., *In situ edge engineering in two-dimensional transition metal dichalcogenides.* Nature communications, 2018. **9**(1): p. 2051.

105.    Li, X., et al., *Suppression of defects and deep levels using isoelectronic tungsten substitution in monolayer MoSe2.* Advanced Functional Materials, 2017. **27**(19): p. 1603850.

**APPENDICES**

## Appendix A

### *Appendix A.1*

**Photoresponsivity (P.R.) spectra of the RGB sensing channels: calculations**

We refer to the equation $R\,(\lambda) = \dfrac{[I_{light} - I_{dark}]}{P(\lambda)}$

Here, $R\,(\lambda)$ refers to spectrum response regarding to wavelength $(\lambda)$, $I_{light}$ refers to excitations current, $I_{dark}$ refers to dark current. $P(\lambda)$ refers the incident light power $P(\lambda)$ as a function of wavelength $\lambda$ of the spectrometer.

### *Appendix A.2*

**Linear dynamic range (LDR): calculations**

We refer to the equation $LDR = 20 \times log_{10}\dfrac{I_{max}}{I_{min}}$

$I_{max}$ refers to highest excitation power in linear I-P figures, $I_{min}$ refers to lowest excitation power in linear I-P figures.

## Appendix B

### *Appendix B.1*

**Dry Transfer Sample Preparation**

We employed blue tape (Nitto SPV224PR-MJ) to successfully exfoliate the vdW-S on the silicon dioxide substrate. In a similar manner, we also achieved the exfoliation of the mica

insulation layer material onto a polydimethylsiloxane (PDMS) film (Gel Pak Gel Film PF-30-X4), which served as the transfer medium.

### Micro Device Fabrication

For the fabrication of miniaturized color sensor, we utilized a custom-built direct laser writing system equipped with a 450 nm diode laser. Kayaku Advanced Material PMGI SF 3S and Kem Lab KL5305 HR are used to form a 100 nm undercut resist and a 300 nm photoresist for UV exposure. Once the coatings were applied, the patterns were obtained by immersing the samples in KL5305 matching developer (Kem Lab TMAH Developer 0.26N) for a duration of 30 seconds. 5/45 nm Ti/Au layers are used to finish metal deposition through thermal evaporation. The final step involved performing a metal lift-off process are finished in acetone solution, resulting in the finished devices.

### Material Characterization

The AFM study was conducted using the Veeco MultiMode V AFM system operating in tapping mode. To capture the photoresponsivity spectra, we collaborated with a source meter unit (SMU, Keithley 2450), a low-noise current preamplifier (Stanford Research System SR570), and an oscilloscope (Tektronix TBS 2000 Series Digital Oscilloscope). For the measurement of I-V and I-P characteristic curves of the RGB components of the color sensor, a home-built high-vacuum probe station equipped with a Keithley 2634B SMU was utilized. Excitation was generated using a Bio-Rad argon-krypton ion laser and a Lexel 85 argon-ion laser at wavelengths of 458 nm, 514 nm, and 647 nm. The intensity of the laser was regulated by two polarizers arranged in series.

### Focus Ion Beam Milling

To obtain three-pixel color sensing array, we carried out Hitachi NB5000 nanoDUE'T FIB-

SEM system for FIB cutting, and a 40 kV gallium (Ga) ion beam was utilized.

### *Appendix B.2*

### Material Synthesis

The monolayer $MoS_2$ crystal in this study was synthesized using the chemical vapor deposition (CVD) method[104, 105]. A 2-inch diameter hinged tube furnace (Lindberg/Blue) was utilized for the synthesis process. Silicon wafers with a 300 nm $SiO_2$ (Si/SiO$_2$) layer were used as the growth substrate. It was spin-coated with perylene-3,4,9,10-tetracarboxylic acid tetrapotassium salt and subsequently dried. The Si/SiO$_2$ wafers were placed face-down above an alumina crucible containing 5g of $MoO_3$ powder (99.9%, Sigma-Aldrich). Another crucible, situated approximately 20 cm upstream from the center of the quartz tube, held around 0.7g of S powder.

Once the tube was evacuated to a pressure of approximately $5\times10^{-3}$ Torr, a mixture of 70 sccm (standard cubic centimeter per minute) of argon and 6 sccm of hydrogen gas was introduced into the tube. The temperature of the furnace was then ramped up to 750 °C at a rate of 30 °C/min and maintained at this temperature for about 4-6 minutes at a pressure of 20 Torr. At 750 °C, the location of the S powder reached approximately 180 °C. After the growth process, the furnace was allowed to cool naturally to room temperature.

### PDMS Preparation

The PDMS precursors required for the study were obtained from Gelest Inc. The PDMS formulation consists of two parts. Part A comprises silanol terminated polydimethylsiloxane (18,000 cSt) with a molecular weight of 77,000g/mol (CAS#70131-67-8), as well as poly(dimethylsiloxane) with a molecular weight of 134.20g/mol (CAS#68412-37-3). On the other hand, part B consists of silicone fluid and di-n-butyldilauryltin with a molecular weight of

631.55g/mol (CAS#77-58-7).

The ratio between part A and part B is 10:1. After mixing, the mixture is placed in a desiccator to remove any air bubbles present. Subsequently, the PDMS filler is poured slowly onto the surface of the sample until it completely covers the desired area. Once the PDMS has cured, it forms a film that can be easily detached from the temporary substrates, while retaining the samples or devices attached to it.